

The Use of Ship-Launched Fixed-Wing UAVs for Measuring the Marine Atmospheric Boundary Layer and Ocean Surface Processes

BENJAMIN D. REINEMAN, LUC LENAIN, AND W. KENDALL MELVILLE

Scripps Institution of Oceanography, La Jolla, California

(Manuscript received 20 January 2015, in final form 6 April 2016)

ABSTRACT

The deployment and recovery of autonomous or remotely piloted platforms from research vessels have become a way of significantly extending the capabilities and reach of the research fleet. This paper describes the use of ship-launched and ship-recovered Boeing–Insitu ScanEagle unmanned aerial vehicles (UAVs). The UAVs were instrumented to characterize the marine atmospheric boundary layer (MABL) structure and dynamics, and to measure ocean surface processes during the October 2012 Equatorial Mixing (EquatorMix) experiment in the central Pacific and during the July 2013 Trident Warrior experiment off the Virginia coast. The UAV measurements, including atmospheric momentum and radiative, sensible, and latent heat fluxes, are complemented by measurements from ship-based instrumentation, including a foremast MABL eddy-covariance system, lidar altimeters, and a digitized X-band radar system. During EquatorMix, UAV measurements reveal longitudinal atmospheric roll structures not sampled by ship measurements, which contribute significantly to vertical fluxes of heat and momentum. With the nadir-looking UAV lidar, surface signatures of internal waves are observed, consistent and coherent with measurements from ship-based X-band radar, a Hydrographic Doppler Sonar System, and a theoretical model. In the Trident Warrior experiment, the instrumented UAVs were used to demonstrate real-time data assimilation of meteorological data from UAVs into regional coupled ocean–atmosphere models. The instrumented UAVs have provided unprecedented spatiotemporal resolution in atmospheric and oceanographic measurements in remote ocean locations, demonstrating the capabilities of these platforms to extend the range and capabilities of the research fleet for oceanographic and atmospheric studies.

1. Introduction

Measurements of sea state and air–sea fluxes have historically been made from ships, buoys, and other platforms, but these essentially fixed-point measurements, over the time scales of surface wave and atmospheric processes, provide no observations of the spatial evolution and distribution of surface fluxes and the wave

field. Aircraft-based measurements are an effective means to sample atmospheric and oceanic phenomena over a wide range of conditions and locations, and are also able to capture the effects of larger-scale structures that may be missed by fixed or slowly moving platforms. There is, however, limited availability of the long range-capable research aircraft required for extended missions or remote locations. Furthermore, the low altitude necessary for accurate atmospheric flux measurements (typically assumed to be 30 m) is below the typical safety limit for sustained flight of a manned aircraft.

Because of advances in electronics and sensor miniaturization, as well as improvements in positioning accuracy and small-aircraft flight control, many research-grade measurements that once required manned aircraft can now be made from small unmanned aerial vehicles (UAVs). In recent years, improved control and guidance technologies have permitted ship launch and recovery of small fixed-wing UAVs, reducing or eliminating transit time for oceanic flights. Pioneered

 Denotes Open Access content.

 Supplemental information related to this paper is available at the Journals Online website: <http://dx.doi.org/10.1175/JTECH-D-15-0019.s1>.

Corresponding author address: Benjamin D. Reineman, Scripps Institution of Oceanography, 9500 Gilman Dr., La Jolla, CA 92093-0213.
E-mail: reineman@ucsd.edu

DOI: 10.1175/JTECH-D-15-0019.1

as a strategy to improve situational awareness at sea, decreased cost and improved reliability of capable platforms permit ship-launched UAVs to make a foray into atmospheric and oceanic research. An overview of maritime UAV operations—past, present, and future—can be found in [de Sousa et al. \(2014\)](#).

In this study, we demonstrate the results from two experiments in which ship-launched UAVs provided spatiotemporal atmospheric and sea surface observations, supplementing and corroborating shipboard measurements of local atmospheric, surface, and subsurface observations. Boeing–Insitu ScanEagles were flown from the R/V *Roger Revelle* as a part of the October 2012 Equatorial Mixing (EquatorMix) experiment. The UAVs provided marine atmospheric boundary layer (MABL) measurements and remote sensing of the sea surface, while instruments operated by other research groups aboard the *Revelle* measured turbulence and mixing in the upper water column. While [Gee et al. \(2008\)](#) used similar ship-based UAVs for geomagnetic surveys, EquatorMix marks the first use of ship-launched and ship-recovered UAVs with payloads for ocean surface observations and atmospheric flux sampling, done in the context of a larger ship-based measurement campaign. Photographs of UAV launch and recovery from the R/V *Roger Revelle* are presented in [Fig. 1](#).

Instrumented ScanEagles were also flown from the R/V *Knorr* during the July 2013 Trident Warrior experiment (TW13; 36.7°N, 75.5°W), where they were used to demonstrate real-time assimilation of UAV meteorological data into a regional coupled ocean–atmosphere model for MABL prediction. This experiment also marked an important milestone in coordinating UAV flights with the operations of a number of other autonomous surface and subsurface platforms.

In this study, we demonstrate the capability of the UAV payloads to explore several phenomena revealed by a novel combination of UAV and shipboard data. We demonstrate the capability of the UAV payloads to collect dense datasets of MABL structure and dynamics with turbulent measurements of wind, temperature, and moisture. With repeated sampling of the MABL, we find evidence of persistent along-wind coherent structures, and quantify their effects on vertical fluxes of momentum and energy. In the context of these structures, we compare ship- and UAV-based sampling strategies.

We also use a combination of UAV- and ship-based instruments to detect surface signatures of internal waves over the coastal Atlantic and in the equatorial Pacific. We demonstrate the capability to identify and track continental shelf internal wave packets using visible imagery transmitted in real time from the UAV, consistent with surface signatures observed with the

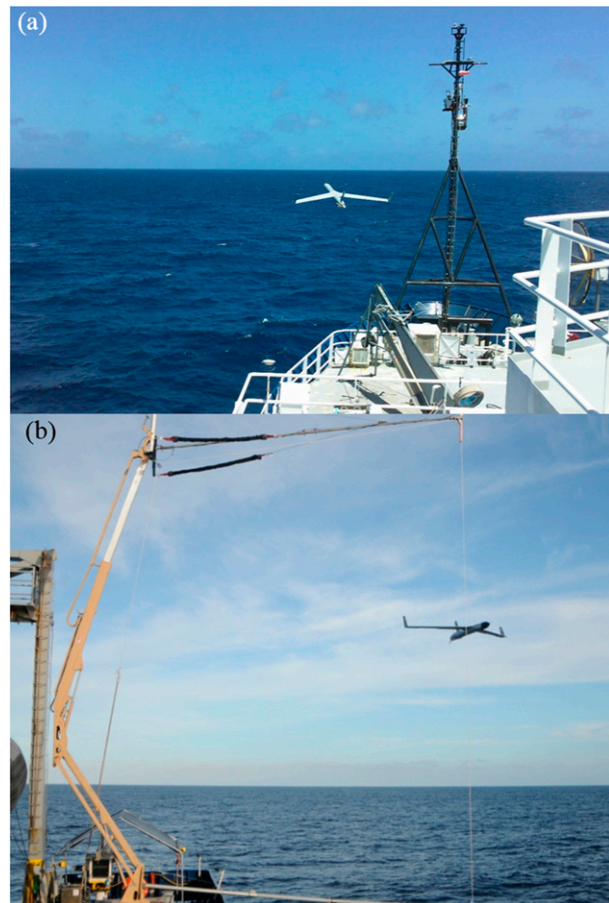


FIG. 1. Photographs of ScanEagle UAV (a) launch and (b) recovery aboard the R/V *Roger Revelle* during EquatorMix [photo (a) courtesy of Jerome Smith].

shipboard radar. At the equator, previous observational studies have examined these phenomena from stationary or towed vertical thermistor arrays (e.g., [Gregg et al. 1985](#); [Moum et al. 1992b, 2011](#)). The present study is distinguished by the fact that it permits the examination of their spatiotemporal structure. This work demonstrates novel ship and airborne measurement techniques of surface signatures of these phenomena, which are considered important in balancing the momentum budget of the equatorial ocean ([Dillon et al. 1989](#)).

In this manuscript we present a description of the UAV payloads, and of flight operations aboard the *Revelle* and the *Knorr*, in [section 2](#). In [section 3](#), we present a description of the ship-based instrumentation. In [section 4](#), we explore the UAV and ship-based measurements of the MABL. In [section 5](#), we investigate ship and UAV observations of internal waves. In [section 6](#), we describe the use of the UAVs for real-time data assimilation in regional atmospheric models. We discuss the results and broader impacts of this technology in [section 7](#).

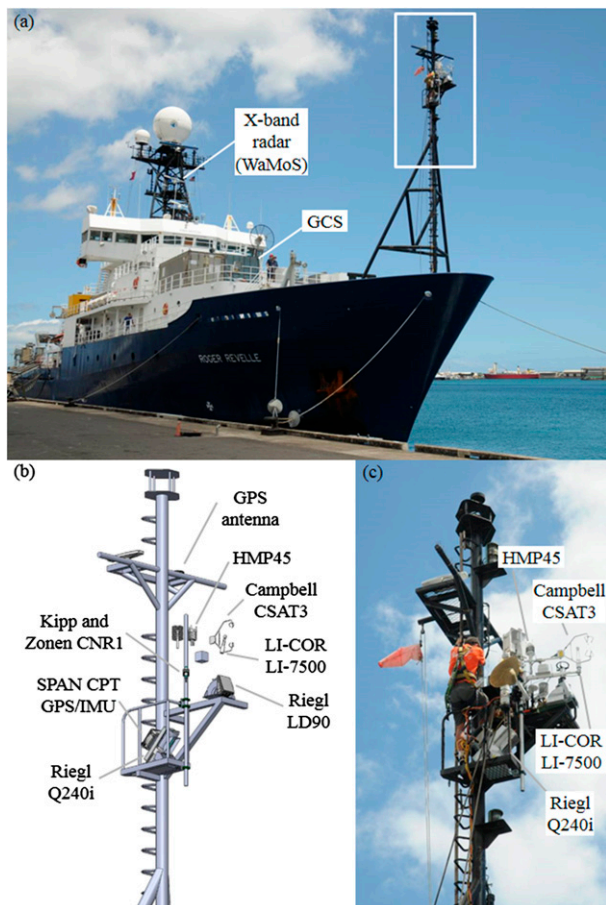


FIG. 2. (a) R/V *Roger Revelle* and (b),(c) instrumented foremast during EquatorMix.

2. UAV payloads, supporting ship-based equipment, and operations

In this section we describe the scientific payloads and then discuss ScanEagle launch, flight, and recovery operations, and the equipment and infrastructure required. A video of at-sea launch, in-flight operations, and recovery can be found in the supplemental materials. During EquatorMix, 11 flights were conducted for 71 total flight hours, with an average flight duration of 6.5 h and a maximum duration of 10.9 h at airspeeds of $25\text{--}28\text{ m s}^{-1}$. General meteorological conditions, measured by instruments on the foremast of the *Revelle* (Fig. 2), are presented in Fig. 3, along with a timeline of UAV flights. During Trident Warrior 2013, 11 flights were conducted over 5 days for 45 flight hours, with an average flight duration of 4.1 h and a maximum of 6.5 h. During both experiments, we conducted overlapping “stacked” flights, with two UAVs in the air in vertically stacked formation: an atmospheric flux-measuring payload at low altitude

(30–90 m), in the field of view of cameras on an imaging payload, flown at 300–900 m.

a. UAV payloads

In both experiments, three UAV science payloads were flown: “Flux,” with fast-response turbulence, temperature, and water vapor sensors, made atmospheric profile and flux measurements; “Radiometric” (RAD) made longwave and shortwave upwelling and downwelling radiation measurements; and “Imaging” (IMAG) recorded visible and infrared imagery. All three payloads perform bulk temperature and relative humidity measurements, and have dedicated radiometric sea surface temperature sensors. An additional “Dummy” payload, with a steerable turret camera, was used in the first flight in each experiment for testing purposes. Table 1 summarizes the measurements performed by the various payloads, gives weight and power specifications, and tabulates flight hours for both experiments. With maximum fuel for the payloads, flights up to 11 h were possible. With only 1–2 h between flights needed for refueling and data transfer, we demonstrated the ability for near-24-h coverage.

The critical sensor for atmospheric flux measurements is the nine-port “turbulence probe,” installed in the Flux payload to measure three-component relative wind. Combined with the onboard coupled GPS–inertial measurement unit (GPS–IMU) and fast-response water vapor and temperature measurements, we can calculate Earth-referenced winds, and momentum, latent, and sensible heat fluxes. Details of turbulence probe calibration and performance, and of all other sensors and payloads, are found in Reineman et al. (2013).

b. Supporting ship equipment for UAV flights

The ScanEagle is launched with a pneumatic catapult, which, for both the *Revelle* and the *Knorr*, was secured on the forward 02 deck (8 m MSL), directed 25° off the bow. The ScanEagles use a unique “SkyHook” recovery system: homing on the location of a GPS antenna at the top of the SkyHook system, the UAV steers the leading edge of the wing into a vertical recovery line. The line slides toward the wing tip, where it is captured by a locking hook mechanism. The SkyHook itself is based on a modified personnel lift that supports upper and lower booms, between which is suspended a 9.5-mm (3/8 in.) nylon rope. The system was secured on the main deck on the aft port quarter, with the end of the upper boom 13 m above the end of the lower boom, which in turn was approximately 2 m above the sea surface. Photographs of the pneumatic launcher (just after a launch) and the SkyHook (just before a recovery) are

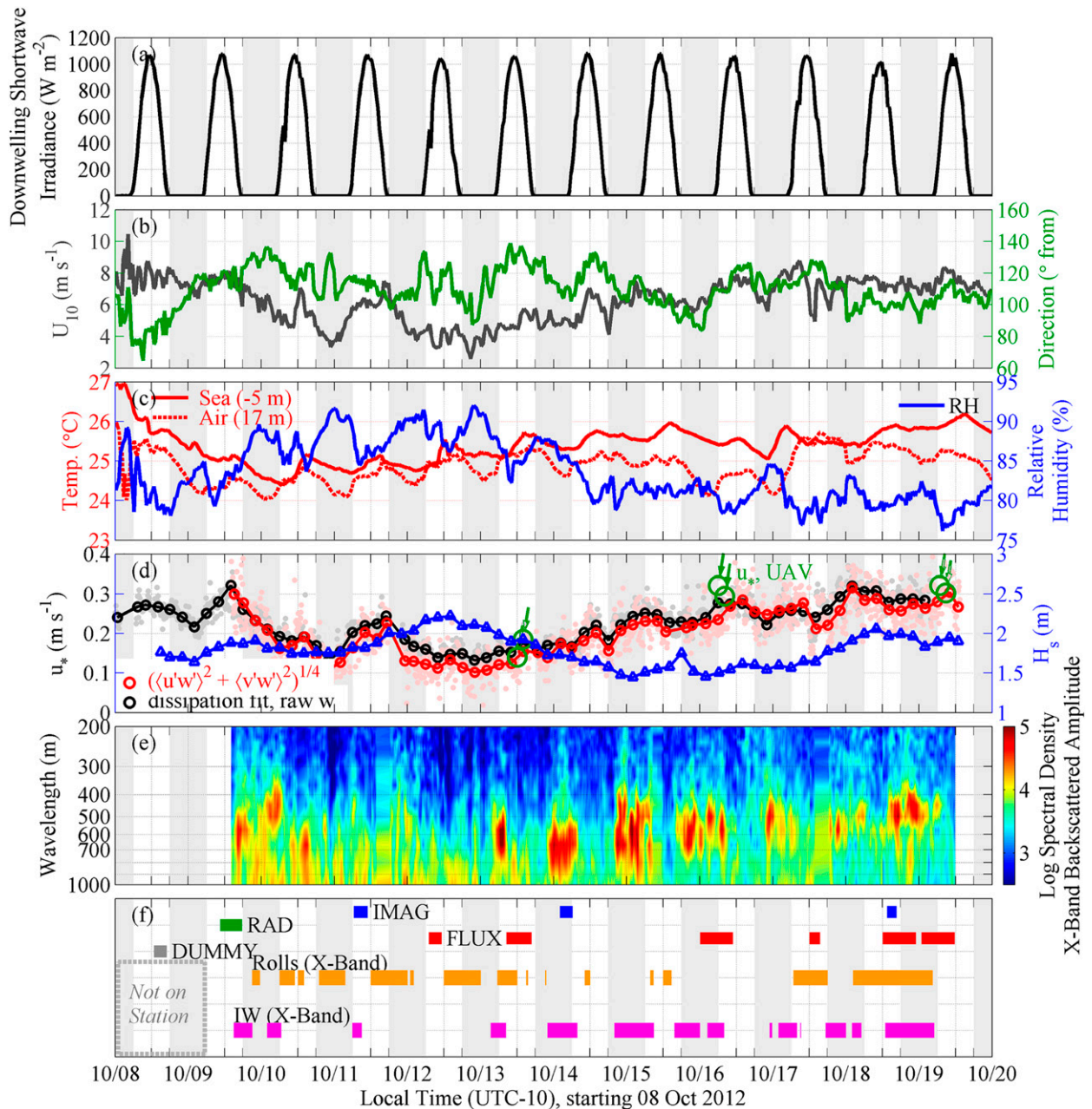


FIG. 3. (a)–(c) Time series of meteorological variables for the duration of the UAV operations during EquatorMix. Solar radiation, air temperature, relative humidity, and wind are measured from the *Revelle* foremast at 17.6 m MSL; sea surface temperature is measured by the ship's thermosalinograph at a depth of approximately 5 m. (d) Friction velocity and significant wave height, the latter calculated from foremast point lidar altimeter. For u_* , black circles are measurements calculated with the sonic anemometer on the foremast from the inertial dissipation method, red circles are from direct eddy-covariance calculations from Earth-referenced winds (using the sonic anemometer and collocated GPS/IMU), and green circles are from low-level (30–60-m MSL) UAV flights. For foremast measurements, light solid markers are from 20-min calculations and larger bold hollow markers denote 6-h averages. (e) Spectrogram of X-band radar backscatter computed from east–west slices, showing power at wavelengths of 400–600 m during times of perceived IW activity. (f) UAV flight table, along with periods where IW or atmospheric roll signatures were observed in the X-band radar imagery.

presented in Fig. 1. Launch and recovery operations are detailed in the following sections.

One 20-ft container was configured as the ground control station (GCS) for the pilots and scientific team,

and a second was used as a maintenance shed for aircraft and parts storage. One pan-and-tilt directional tracking antenna was positioned on top of the GCS, and another was installed aft of the bridge. An

TABLE 1. Measurement summary for ScanEagle payloads (“Flux,” “Radiometric,” and “Imaging”) used in EquatorMix (EQ) and TW13. Payload weight includes sensors, acquisition electronics and wiring, and internal aluminum framing. Total flights and flight hours from each experiment are noted. Adapted from Reineman et al. (2013), where tabulated details of sensors can also be found.

Measurement	Payload		
	FLUX	RAD	IMAG
3D wind, flux measurements	Yes	No	No
Fast-response temperature, water vapor	Yes	No	No
Slow-response temperature, relative humidity	Yes	Yes	Yes
Shortwave/longwave, upwelling/downwelling radiation	No	Yes	No
High-resolution nadir visible imagery	No	Yes	Yes
Infrared imagery	No	No	Yes
Nadir point lidar altimeter	Yes	No	Yes
Sea surface temperature	Yes	Yes	Yes
Payload weight (kg)	3.1	1.9	2.1
Payload power (W)	33	23	32
	EQ, TW13	EQ, TW13	EQ, TW13
Total flights	6, 7	1, 1	3, 2
Total flight hours	48.0, 34.6	7.1, 1.9	11.4, 5.3

omnidirectional antenna, for close-range communication, was also installed near each directional antenna. Details and schematics of equipment layout on the *Revelle* (similar to the configuration on the *Knorr*) can be found in Reineman (2013).

c. Prelaunch and launch

During the prelaunch sequence, UAV pilots and operators adhere to an extensive safety and operation checklist for the aircraft. Additionally, the scientific party followed a separate sensor and communications checklist for the scientific payload. This checklist included verification of pneumatic-tube pressure connections in the turbulence probe, cleaning of optical sensors (fast-response hygrometer, nadir lidar) and camera lenses, and testing of all data and communication links. The engine is started and run through a range of throttle settings to ensure it is running smoothly. Separate cooling airflow over the engine can be turned off and on as needed while on the launcher, allowing the air-cooled engine to be run indefinitely while the UAV is stationary.

In preparation for launch, ship course and speed are directed to give relative winds of approximately 10–20 kt (5–10 ms⁻¹) aligned with the launcher. The relative wind speed and UAV takeoff weight determine the

pressure required by the launcher’s pneumatic cylinder, which is pressurized just before launch. Once the pilot gives the command, a manual launch cord is pulled by a launch operator. After a few minutes of in-flight system and performance checks, the UAV is ready for its scientific mission.

d. In flight

Aircraft control is autonomous, with the pilot prescribing waypoints, altitudes, descent and ascent rates, and airspeed via a graphical interface. Missions can be configured ahead of time, but more often, a rough mission outline is predetermined, and the UAV is directed “on the fly.” Specific lost-communication holding patterns and engine failure-induced ditch areas are prescribed a priori, and are relocated as necessary so as to follow the moving vessel. At least one pilot is always stationed in the GCS, monitoring and directing the flight paths. For extended flights, pilots rotate through 2-h shifts.

During flights, the science party stationed in the GCS monitored real-time atmospheric data (1-Hz averaged data were transmitted through the line-of-sight communications link) and provided flight directives to the pilots. Graphical monitoring included time series of atmospheric data, the most recent vertical profiles of temperature and relative humidity, and real-time 3D trajectory plotting in Google Earth, with a color scale prescribable to any of the measured atmospheric data variables. A sample 3D trajectory of one 11-h flight during EquatorMix is presented in Fig. 4. Science missions were directed well upwind or abeam of the ship so that measured winds were not influenced by the vessel, a distinct advantage compared to atmospheric measurements from the vessel itself. Communication range is stated as 100-km line of sight, and with the UAV at 30 m we found communication up to 30 or 40 km was attainable.

Though small amounts of precipitation did not interfere with aircraft control, we attempted to avoid precipitation and cloud formations when possible by watching the nose camera video stream. During night operations, we typically kept the UAV below the observed cloud ceiling (approximately 500 m for EquatorMix). We monitored time series of turbulence probe individual pressure sensors, which on several occasions showed evidence of water obstruction that would typically clear in less than 10 min of flying in dry air.

During vertically stacked flights, the ScanEagles required one complete pilot station per aircraft (a separate flight computer was configured in the GCS, with separate tracking and omnidirectional antennas), with a dedicated pilot for each. Waypoints were shared across

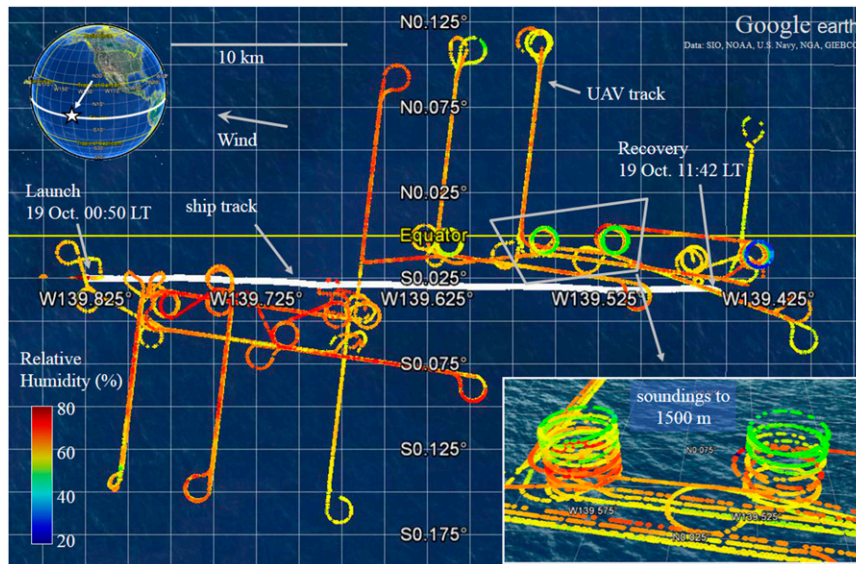


FIG. 4. Sample 1-Hz real-time data in Google Earth during one 11-h flight (19 Oct 2021) in EquatorMix (0.0°N, 139.6°W). Color scale can be chosen to correspond to altitude or to any measured atmospheric variable, in this case relative humidity. The ship track is shown in white, traversing eastward throughout the flight. (inset) A perspective view of two helical vertical soundings.

a network between the two stations, and stacked formation was achieved through careful adjustments to course and airspeed.¹

During the Trident Warrior experiment, as a safety measure, an Automatic Identification System (AIS) transmitter was installed in the ScanEagle GCS, broadcasting the position and altitude of the UAV in real time. The signal was purposely highly attenuated such that it could be visible only by the *Knorr*'s AIS receiver. The bridge of the *Knorr* was then able to monitor the position of the UAV on radar displays (along with other AIS-broadcasting vessels) without additional infrastructure. The radar was repeated on a dedicated screen inside the GCS, allowing pilots to monitor ship traffic.

e. Recovery

Recovery is an autonomous operation, which uses the positions of the UAV's GPS and the GPS antenna mounted on the SkyHook's upper boom in line with the capture line. In preparation, ship course and speed are directed to give relative winds of approximately 10–20 kt (5–10 m s⁻¹) from 15° off the port bow, in line with the approach vector. During recovery, one dedicated

spotter makes the call to abort if the approach vector appears abnormal. The pilot has the option to abort the capture and “wave-off” at any time outside 5 s from anticipated recovery. Though a particular location on the starboard (ship-ward) wing is specified where the vertical line should first contact, the airframe is designed to accept a line hit anywhere on the span of either wing. The engine is automatically shut down when the inertial measurement unit registers a high yaw rate, which occurs upon capture. For all SkyHook recoveries in these experiments, there was never an unplanned wave-off or a missed capture. This was facilitated by the low winds ($U_{10} < 10 \text{ m s}^{-1}$) and calm seas (significant wave height $H_s < 3 \text{ m}$) experienced throughout the experiments.

After capture, the UAV is hoisted up to the upper boom to limit vessel- and wind-induced motion. The SkyHook is then rotated inboard, the lower boom is lifted over the bulwark, and the upper boom is lowered until the ScanEagle can be secured manually by the deck crew. The ScanEagle is then unhooked, carried to its stand, and defueled. Data backup can be completed either wirelessly (over an ad hoc network), or over USB to an external drive. The latter is required for the larger imaging datasets.

Every attempted capture for these experiments was successful. In one flight during EquatorMix, however, a faulty avionics airspeed sensor forced a controlled water landing that resulted in the loss of the Radiometric

¹This was in contrast to previous work in which multiple BAE Manta platforms were controlled from one ground station (Reineman et al. 2013).

payload (8 October 2012).² During another recovery (16 October 2012), the UAV captured too low on the line and struck the lower boom, resulting in minor but repairable damage.

3. Ship-based instrumentation

a. Foremast meteorological and remote sensing instruments

During EquatorMix, a sonic anemometer-based eddy-covariance system, with a Campbell Scientific CSAT3 and LI-COR LI-7500, for water vapor measurements, was installed on the *Revelle* foremast (Fig. 2). A NovAtel Synchronous Position, Attitude and Navigation (SPAN) CPT GPS/IMU was mounted on the mast adjacent to the instruments. Position, orientation, and velocity data are computed in postprocessing in NovAtel Inertial Explorer software, using “precise point positioning” (PPP) for improved positioning using refined GPS clock and orbit files (publicly available online with approximately 1-day latency). Velocity rms accuracies after postprocessing are estimated to be 2 cm s^{-1} in the horizontal and 1 cm s^{-1} in the vertical, and position accuracies are 1 and 2 cm, respectively.³

The three-component wind is rotated into an Earth reference frame with the GPS/IMU data. While this removes most of the effect of the relative wind induced by the ship motion, there is still contamination due to the presence of the vessel itself. This is a persistent problem with ship-based flux measurements, and it has been examined in detail in previous studies (e.g., Oost et al. 1994; Yelland et al. 1998; Edson et al. 1998). We retain the ship-based measurements in our analysis for comparison with measurements from the UAVs—platforms that have the potential to overcome these issues with accurate sampling of the uncontaminated MABL.

Direct eddy covariance fluxes from the foremast are calculated (and detrended) over a 20-min averaging time, corresponding to spatial scales of 5–12 km, assuming mean wind speeds of $4\text{--}10\text{ m s}^{-1}$ (and upwind ship speed of 1 m s^{-1}). Friction velocity is computed as

²The water landing was rougher than anticipated, and though the airframe was recovered (having sustained moderate damage), the payload and nose section separated from the fuselage on impact and sank. An identical replacement payload was built for Trident Warrior 2013.

³This is the same position and velocity accuracy expected by the NovAtel SPAN LN200 GPS/IMU aboard the Flux payload, as discussed in Reineman et al. (2013), though now also using precise point positioning GPS corrections. The fiber-optic LN200-based SPAN has significantly better attitude performance, which is critical for Earth-referencing winds in the fast-moving UAV.

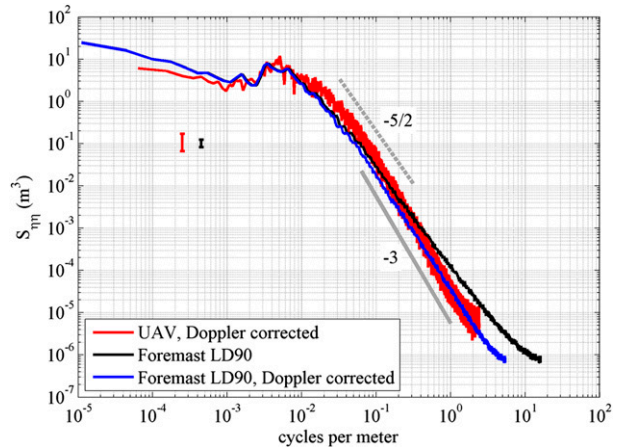


FIG. 5. Surface wave spectra, from the 12-h period beginning 18 Oct 1200 LT, during EquatorMix. For the UAVs, the spectrum is computed with 34 segments, each 5.5 km upwind, measured from below 100 m MSL. For the foremast LD90 point lidar altimeter, the spectrum is computed from 5-min windows and then it is shifted into wavenumber space and corrected for the speed of the ship (1 m s^{-1} , off the wind by $10^\circ\text{--}15^\circ$). Slopes of -3 (saturation spectrum) and $-5/2$ (equilibrium spectrum) are shown.

$$u_* = (\langle u'w' \rangle^2 + \langle v'w' \rangle^2)^{1/4}, \quad (1)$$

where u and v are the horizontal wind components, respectively; w is the vertical component, and u is aligned with the mean wind direction over the 20-min record. Primes indicate turbulent quantities, and angle brackets are time averages. Friction velocity is also calculated by the inertial dissipation method using the raw (not Earth referenced) vertical velocity spectra, fitting a $-5/3$ inertial subrange to the 20-min spectrum over 0.3–3 Hz. These frequencies are higher than the $O(10)$ -s period of ship motion (see, e.g., Jones and Toba 2001). The estimate from this dissipation method, averaged over data from this experiment, is seen to be systematically 0.018 m s^{-1} higher (an 11% absolute bias on average) than that from the direct Reynold’s stress measurement of (1) (Fig. 3d).

A Riegl LD90 (point lidar) and Q240i (fore–aft scanning lidar) were also mounted on the *Revelle* foremast for surface wave measurements. Sample surface elevation wavenumber spectra from the foremast point lidar (Earth referenced with the SPAN GPS/IMU; cf. Reineman et al. 2009) are presented in Fig. 5. Spectra are Doppler corrected for the movement of the ship and then transformed into wavenumber space using the linear deep-water dispersion relation. There is good agreement between the spectra measured by the foremast and those measured by the UAV laser altimeter.

b. X-band marine radar

X-band marine radars can be equipped with digitizing and logging capabilities—for example, the Wave

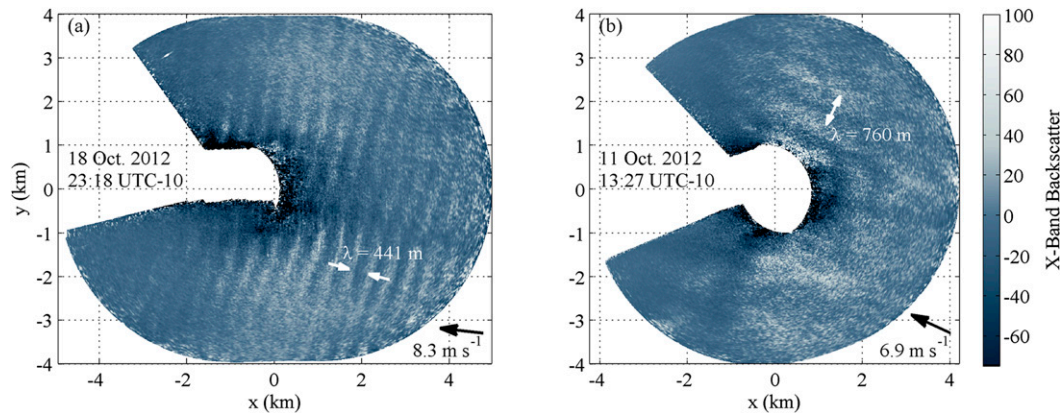


FIG. 6. Examples of surface features seen in Earth-referenced, time-averaged X-band radar imagery measured with WaMoS aboard the R/V *Revelle* during EquatorMix. (a) Crosswind surface signatures of IWs, computed with a 30-min average of georeferenced X-band imagery. IW phase speed at this time is near zero (see Fig. 17), allowing for long-term (30 min) averaging without “smearing” the signal. (b) Along-wind surface signatures of atmospheric rolls, computed with a 10-min average of georeferenced X-band imagery. Wind vectors (black arrows) shown are measured at the *Revelle* foremast.

Monitoring System (WaMoS; <http://www.oceanwaves.de/>), a system developed for the estimation of surface wave directional spectra and surface currents (the latter by inverting the surface wave dispersion relation; see, e.g., Nieto Borge et al. 2004). WaMoS has been installed on a number of University–National Oceanographic Laboratory System (UNOLS)-managed U.S. research vessels. Though mainly intended for surface wave and current extraction (similarly, inversion for shallow-water bathymetry has also been demonstrated; see, e.g., Bell 1999; Hessner et al. 2014), by averaging out the surface gravity waves, X-band radar can be used to reveal persistent surface features, notably the surface signatures of internal waves (e.g., Ramos et al. 2009; Lund et al. 2013). Slight modulations in surface currents, as well as converging and diverging surfactants, affect the $O(1)$ -cm surface wavefield—wavelengths at which X-band radar returns (sea clutter) are very sensitive.

WaMoS, which uses a Furuno FAR-2117 BB marine radar, is installed on the *Revelle*. The system was continuously recording 12-bit images at 42 frames per minute throughout the experiment; each frame was digitized with a resolution of 5 mrad (0.284°) azimuthally and 7.5 m radially, out to a 4-km range (resulting in approximately 7.5×20 m boxes at 4 km). Following Ramos et al. (2009), data are corrected for azimuthal and range signal dependence. Data aft of the ship (145° – 215° , assuming the bow is aligned with 0°) is blocked by the ship’s main mast (see Fig. 2), and a narrow band of data straight forward is obscured by the foremast. Data are converted into an Earth reference frame using the ship’s gyrocompass and GPS and then interpolated onto a 10-m grid. To reveal slowly moving features,

we compute time averages of the Earth-referenced imagery over several minutes. Higher-frequency features, such as surface waves, are thus removed. Sample Earth-referenced and time-averaged X-band images are shown in Fig. 6, which give examples of phenomena to be discussed in detail in subsequent sections.

c. Subsurface instrumentation

A high-resolution Hydrographic Doppler Sonar System (HDSS) is installed on the *Revelle* (Pinkel et al. 2003), consisting of 50- and 140-kHz systems. Each of the four beams is oriented 30° from vertical. The 140-kHz system provides three-component velocity in 3-m vertical bins down to about 250 m (where noise overwhelms the signal during EquatorMix) averaged over 1-min intervals, while the 50-kHz system reaches about 600 m in 14-m bins.

A rapidly profiling “fastCTD” (e.g., Rainville and Pinkel 2006) was deployed from the *Revelle* for a majority of the time during EquatorMix, profiling to 300 m every 3 min, punctuated by deep casts to 1500 m every 6 h. Data from the HDSS and FastCTD are used to identify the subsurface structure of internal waves, surface signatures of which we find in UAV and X-band radar data, as discussed in section 5.

4. Examples of MABL structure and dynamics

a. Vertical structure

Evolution of vertical atmospheric structure, as measured by helical vertical soundings, during EquatorMix over 13–19 October 2012 is presented in Fig. 7,

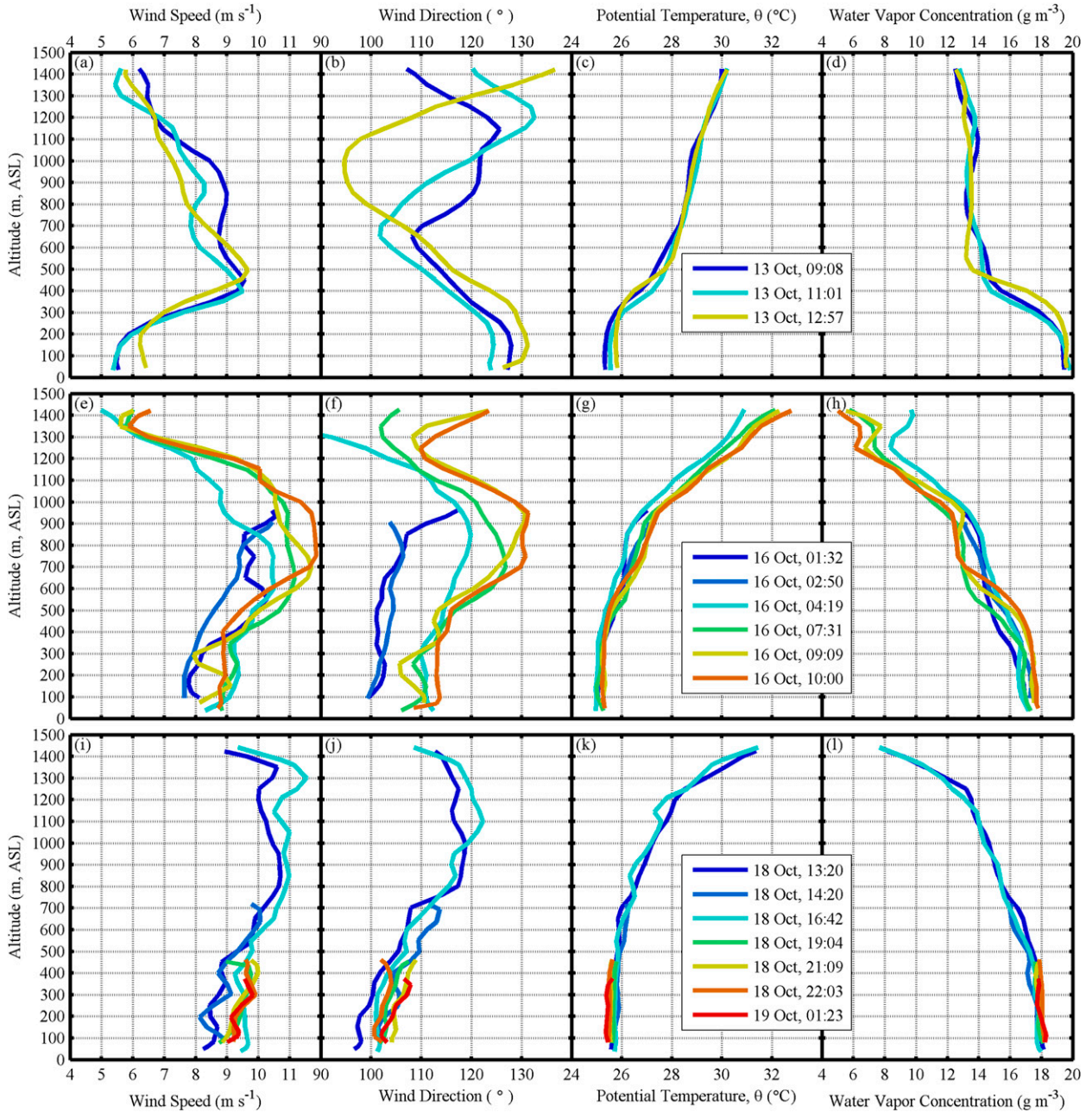


FIG. 7. (left to right) Vertical profiles of wind speed, wind direction (from), potential temperature, and water vapor concentration, computed from helical vertical soundings made by the Flux payload throughout EquatorMix. Data are averaged into 100-m vertical bins with 50% overlap; orbit diameter is 1 km. Profiles are then reduced by binning into 2-h intervals (LT given). During night operations, profiles were typically capped at 500 m.

binned in space and time for clarity. Winds under 300 m increased over the course of the experiment. A jet is visible at about 500 m on 13 October and then at 700–900 m on 16 October, and a well-mixed layer in the bottom few hundred meters is prominent throughout, increasing from 300 m on 13 October to 550 m on 19 October.

b. Observations of atmospheric rolls

Longitudinal rolls (helical structures oriented along wind) in the atmospheric boundary layer are a common feature with potentially a large influence on turbulent transport (Etiling and Brown 1993). Figure 8 visualizes this phenomenon conceptually. Previous investigations

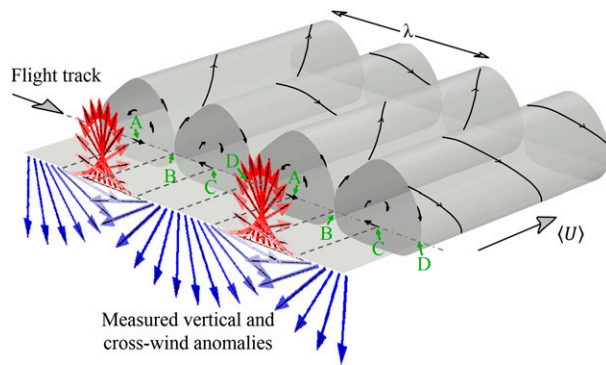


FIG. 8. Schematic of idealized longitudinal helical paired roll structures of λ in the MABL. The mean wind (U) is in the direction shown. Also shown are idealized local vertical and crosswind components as measured by a hypothetical aircraft transect across the rolls (flying below the center of roll rotation). There is a 90° phase shift between the components: at location A, true wind as seen by the UAV is in the direction of flight; at location B, true wind is up; at location C, wind is against the direction of flight; and at location D, wind is down. Color corresponds to the vertical wind component, from negative (blue) to positive (red).

have shown they are visible in satellite synthetic aperture radar (SAR) imagery because of the sea surface roughness modulations induced by slight wind variations (e.g., Sikora and Ufermann 2004; Chen et al. 2001). Similarly, in this study, we often see evidence

of roll structures in the X-band radar as along-wind streaks with transverse wavelengths of 1–2 km (Fig. 6b). Times of clear roll-like X-band signatures are charted in Fig. 3f.

Several airborne studies have documented such helical structures in the MABL (e.g., Hein and Brown 1988; Brooks and Rogers 1997; Chen et al. 2001). When flying through the helical structures in a crosswind direction, we would expect to see a 90° phase shift between vertical and crosswind wind components, as is depicted schematically in Fig. 8. A 90° phase difference between vertical and crosswind components is observed in the time series of 30–100-m altitude flights during the two 11-h back-to-back flights over 18–19 October. Wind components also show a striking coherence between vertical wind, moisture, and temperature (Fig. 9), resulting in the positive latent and sensible heat fluxes quantified in section 4c.

The v and w phase difference is quantified spectrally, considering all straight-and-level legs under 200 m from 18 to 19 October in Fig. 10, which shows a tendency toward $\pm 90^\circ$ at low wavenumbers in crosswind flights, with the sign dependent on the crosswind sampling direction. As noted by Hein and Brown (1988) and Chen et al. (2001), the $\pm 90^\circ$ phase behavior in crosswind sampling is an indicator of helical structures with axes aligned roughly with the mean wind. This coherence is

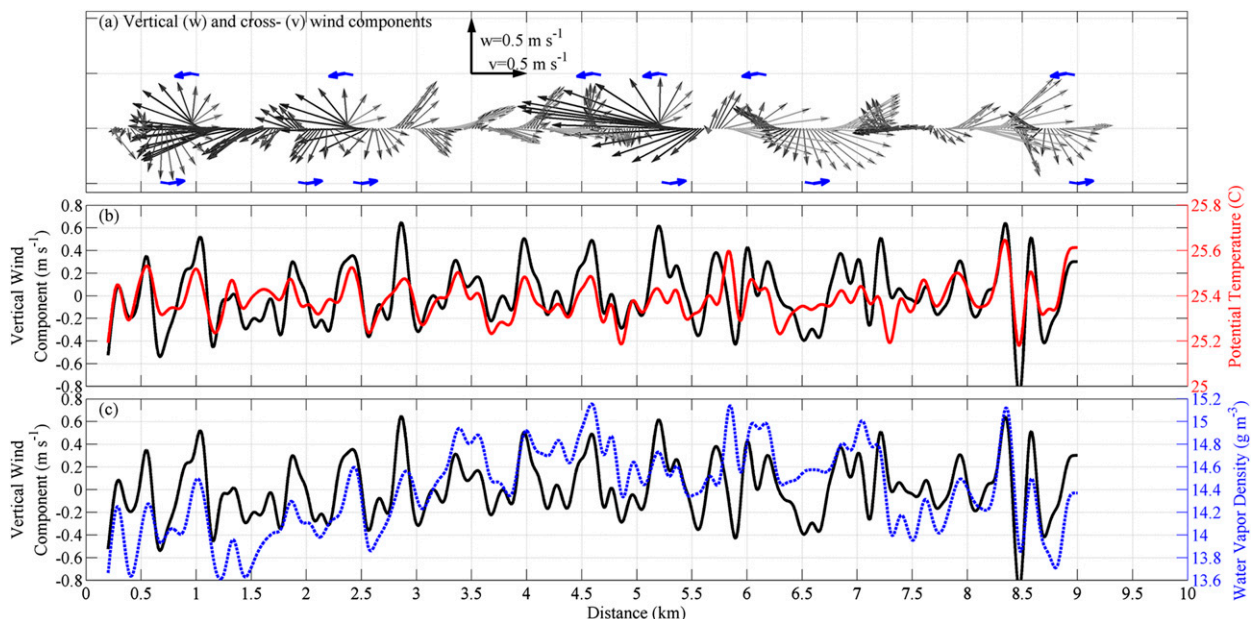


FIG. 9. Time series from a low-level (60-m altitude) crosswind flight segment through the boundary layer during EquatorMix, starting 0147 LT 19 Oct, showing (a) vertical and crosswind anomalies in a “quiver” plot, (b) potential temperature and vertical wind, and (c) water vapor density and vertical wind. Time series (b) and (c) are low-pass filtered with a 3-s (85 m) cutoff; the winds in the quiver plot are low-pass filtered with a 5-s (140 m) cutoff and an arrow is shown every 1 s, for clarity. Small blue arrows are added in (a) to help visualize the direction that the wind vectors are turning.

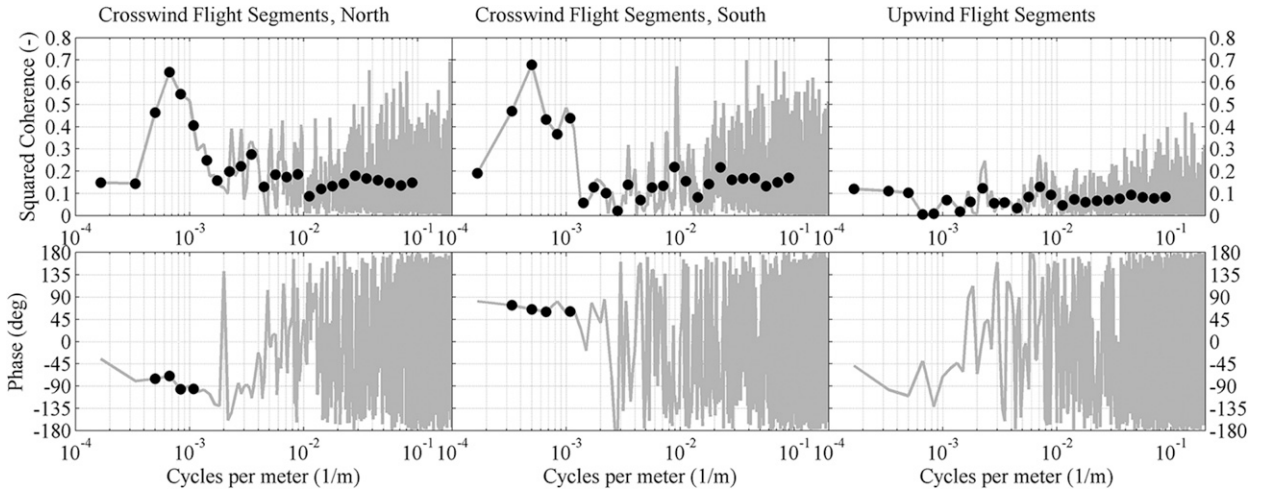


FIG. 10. Squared coherence and phase between cross- and vertical wind components, computed from all straight-and-level flight segments (using 6-km spectral windowing) between 30 and 200 m MSL for the 24-h period beginning 1200 LT (UTC – 10 h) on 19 Oct 2012, during EquatorMix (in the vicinity of 0°N, 140°W). Note the coherence at wavenumbers corresponding to 1–2.5 km in the crosswind flight segments, and the corresponding phase approaching $\pm 90^\circ$, with the sign dependent on the crosswind flight direction. The significant differences in coherence and phase between the upwind and crosswind segments are very clear.

not discernible in the along-wind flight segments. The squared coherence (Figs. 10a–c) suggests these features have wavelengths of 1–2.5 km. If we assume the height of these features to be $h = 450\text{--}550$ m, corresponding to the top of the well-mixed layer seen in Fig. 7d, then we compute aspect ratios of $\lambda/h \approx 2\text{--}5$, which agree with the theoretical value of $\lambda/h = 2$ derived by Brown (1970) for neutral stratification, and in the range of previous observations ($\lambda/h = 2\text{--}6$ in the majority of studies compiled by Kelly 1984) and numerical simulations (Sullivan et al. 2014).

c. Turbulent measurements and flux calculations

Spectra of wind components, temperature, and water vapor density from all 10-km straight-and-level legs of the 11-h flight on 16 October are presented in Fig. 11, grouped by flight altitude and sampling direction and binned in frequency for clarity. The turbulence probe is seen to capture the inertial subrange of the turbulence down to wavelengths of $\lambda \approx 0.4$ m. More energy is seen at all wavelengths for lower legs, with the exception of temperature and moisture spectra at 395 m, coinciding with high temperature and moisture gradients seen in Figs. 7g,h. Fluxes are quantified with integrated cospectra, as described first by Friehe et al. (1991), and in the context of UAV measurements by Reineman et al. (2013). Mean cumulative cospectra corresponding to vertical flux of along- and crosswind momentum, latent heat flux, and sensible heat flux, again grouped by flight altitude and sampling direction, are shown in Fig. 12.

Figure 13 presents a timeline of flux measurements from all 30–60-m altitude legs during the period 13–19 October 2012 (differences in fluxes between 30 and 60 m are within measurement standard errors). The Webb effect (Webb et al. 1980; Fairall et al. 1996) is included in the calculation, which accounts for $0.5\text{--}7\text{ W m}^{-2}$ (3%–5%) of the latent heat flux. Fluxes measured during crosswind flight segments are notably larger than those measured during upwind and downwind segments, as expected due to the presence of the roll structures described in the previous section. We consider 6-h bin averages of the flux measurements to allow for direct comparisons between measurements from the different sampling directions and the foremast measurements, shown compared with a 1:1 line in Fig. 14. Fluxes from crosswind sampling are larger than those from along-wind sampling by 20% (momentum flux), 8% (u_*), 15% (latent heat flux), and 55% (sensible heat flux), as indicated by the gray markers in the inset plots of Fig. 14. There are similar differences between measurements from crosswind UAV sampling and those computed from the foremast eddy-covariance station (red triangles in Fig. 14). Error bars indicate ± 1 standard error within the 6-h bins.

Vertical profiles of fluxes are presented in Fig. 15, with altitude-binned fluxes from all straight-and-level flights. We focus on these two flight periods as they show two clear regimes: one from low-wind conditions ($U_{10} = 5\text{ m s}^{-1}$), with a shallower boundary layer (300 m), and one from higher winds ($U_{10} = 7\text{--}8\text{ m s}^{-1}$), with a higher boundary layer (900 m). We also include

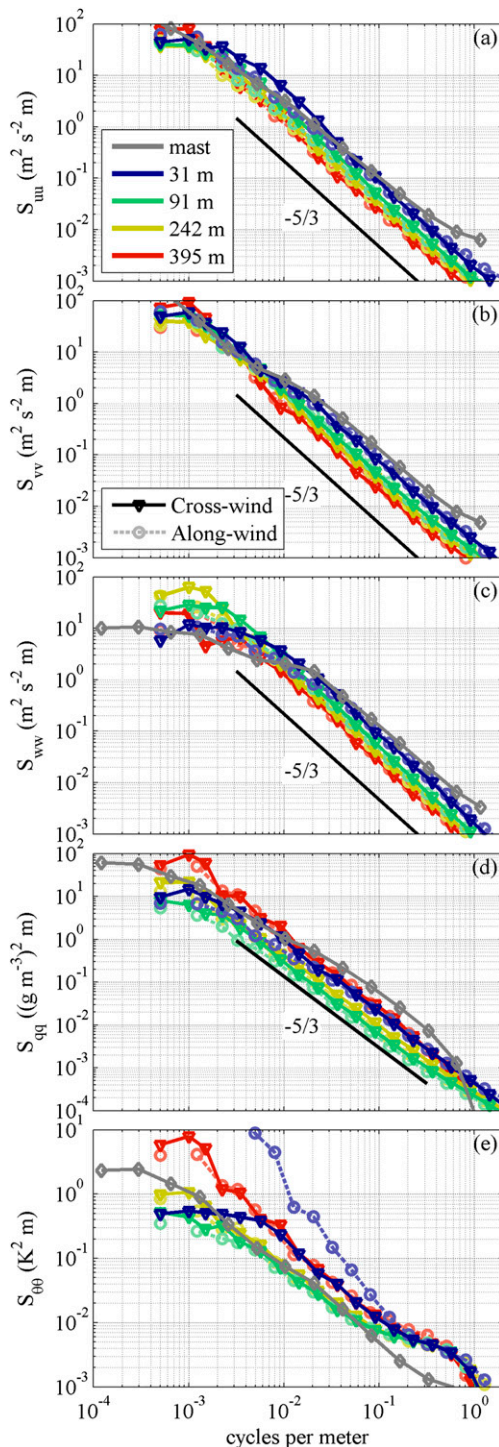


FIG. 11. Spectra of (a)–(c) wind components (u , v , w), (d) water vapor density, and (e) temperature measured during straight-and-level UAV legs (colors) for the 11-h period starting at 0000 LT 16 Oct 2012, generated from 2-km segments, during EquatorMix. Darker solid curves are from crosswind segments and lighter dotted curves are from along-wind segments (upwind and downwind). Gray curves are computed from the eddy-covariance station on the foremast (17.6 m MSL) of the *Revelle*, using 20-min segments, averaged over the same 11-h period, and shifted into wavenumber space using the mean wind speed (assuming frozen turbulence).

fluxes measured from within helical vertical soundings (Reineman et al. 2013), which, though they are expected to underestimate the flux by 15%–50% as they do not capture contributions of scales larger than the 1-km orbit diameter (estimated by examining the crosswind gives values at 1 km^{-1} compared to their values at $1/8 \text{ km}^{-1}$ in Fig. 12), they do reveal the vertical flux structure above the highest straight-and-level measurements. Larger orbit diameters are expected to capture these larger-scale structures. Fluxes computed from the 17.6-m eddy-covariance station on the foremast are included, averaged from the 20-min segments of the corresponding sampling time. As was seen in Figs. 13 and 14, the foremast eddy-covariance flux measurements are an underestimate: they are smaller in magnitude and more in agreement with the along-wind measurements rather than the crosswind measurements, especially for the windier conditions on 18–19 October 2012. Larger fluxes are seen closer to the surface, with magnitudes dropping to near zero above the boundary layer (Fig. 7). There is a marked increase in the magnitude of fluxes at all altitudes within the boundary layer between 13 and 18 October 2012.

The density of atmospheric turbulence data and flux measurements (in time and vertical space) in a central ocean basin, as demonstrated here, is difficult to obtain with traditional flux measurement methods from manned aircraft or research vessels. Additionally, crosswind spatial sampling over extended periods in these remote locations, which reveals significantly larger fluxes associated with atmospheric rolls, may be achievable only with ship-launched UAV technology.

5. Examples of coincident ship- and UAV-based observations of internal waves

In this section we present observations of internal waves (IWs) from the equatorial Pacific and the Atlantic continental shelf from UAV- and ship-based instrumentation. The present study is unique in that we use both UAV and ship measurements to examine IW temporal and spatial structure (specifically, examining the surface manifestations of the internal dynamics), whereas traditional local observations from research vessels often have difficulty resolving temporal from spatial variability.

a. Ship- and UAV-based observations of coastal internal waves

During TW13, there were a number of identifiable incidences of packets of internal waves visible in images from the ship, from the forward-looking UAV navigation cameras and from the nadir-looking UAV cameras.

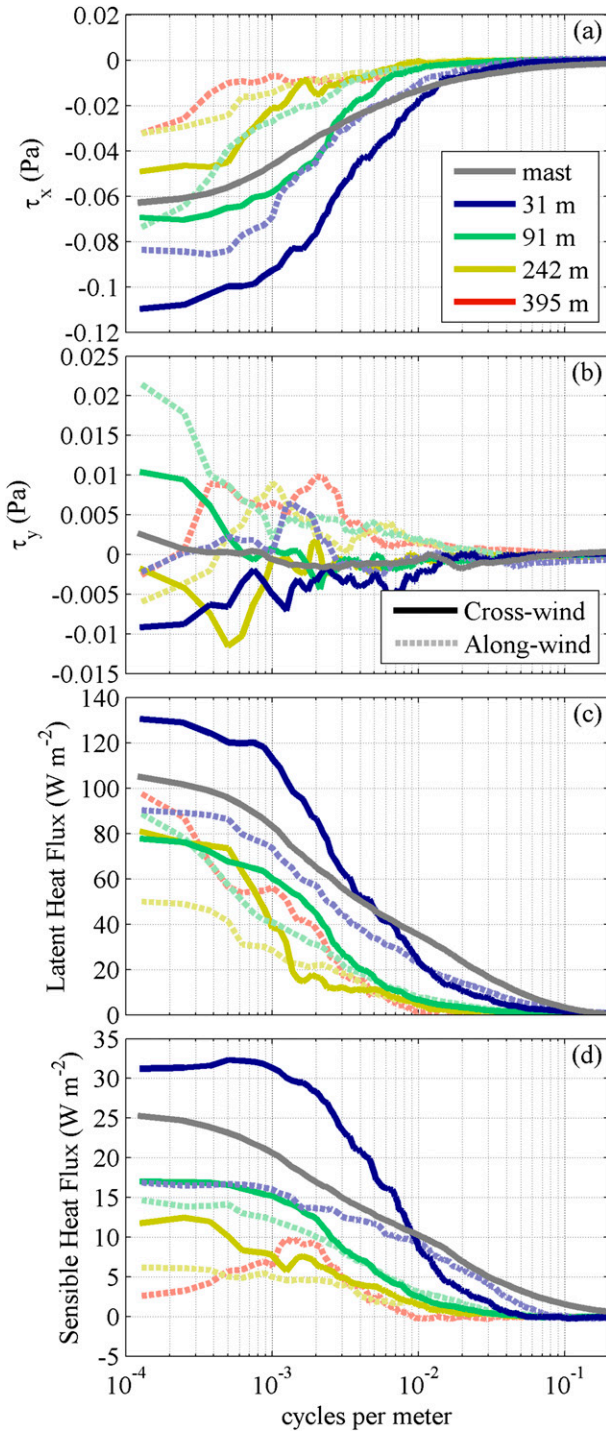


FIG. 12. Integrated cospectra (“ogives”) computed from straight-and-level UAV legs (colors), corresponding to (a) along-wind momentum flux, (b) crosswind momentum flux, (c) latent heat flux, and (d) sensible heat flux. Ogives are computed from 8-km segments for the 11-h period starting at 0000 LT 16 Oct 2012, during EquatorMix. Darker solid curves are from crosswind segments and lighter dotted curves are from along-wind segments. Gray curves are as in Fig. 11. The large latent heat flux at 395 m is associated with the strong gradient in water vapor seen in Fig. 7h.

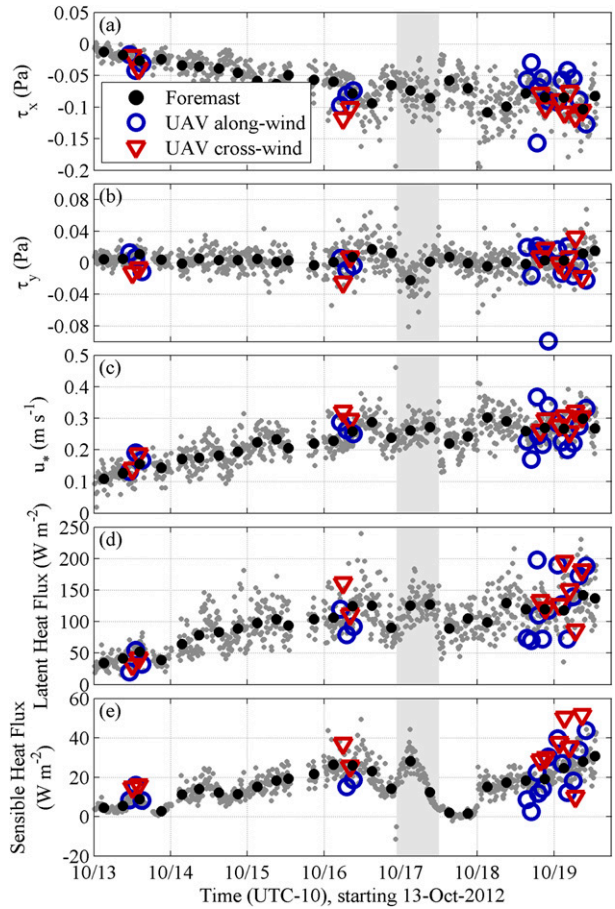


FIG. 13. Time series of (a) along-wind momentum flux τ_x , (b) crosswind momentum flux τ_y , (c) friction velocity u_* , (d) latent heat flux Q_L , and (e) sensible heat flux Q_S as measured by low-altitude (30–60 m) UAV flights (colors) and by the eddy-covariance station on the foremast (gray and black), during EquatorMix. Solid black circles represent 6-h bin averages of foremast measurements. Crosswind UAV legs are denoted by red triangles and along-wind UAV legs are denoted by blue circles. Spectral windows of 8 km are used for the UAV flux calculations and 20 min for the foremast (corresponding to 5–11 km when considering the mean measured wind of 4–9 m s⁻¹). The light gray bars indicate a time of fast (13 kt) westward (downwind) transit, when foremast measurements are in the wind wake of the vessel.

The visibility of these phenomena was lighting dependent, and they were manifested as bands of “slicks” in sun glitter (e.g., Wang and Pawlowicz 2012). Packets were also identifiable in the marine X-band radar. *Knorr* was not equipped with a radar digitizing and logging device (e.g., WaMoS), but photographs of the radar plan position indicator (PPI) display documented several of these events. Qualitative examples of internal wave packet observations are shown in Fig. 16. Internal wave packets have been documented and studied in this Mid-Atlantic Bight region over the years, both from satellite imagery (e.g., Jackson 2007) and from SAR (e.g., Porter

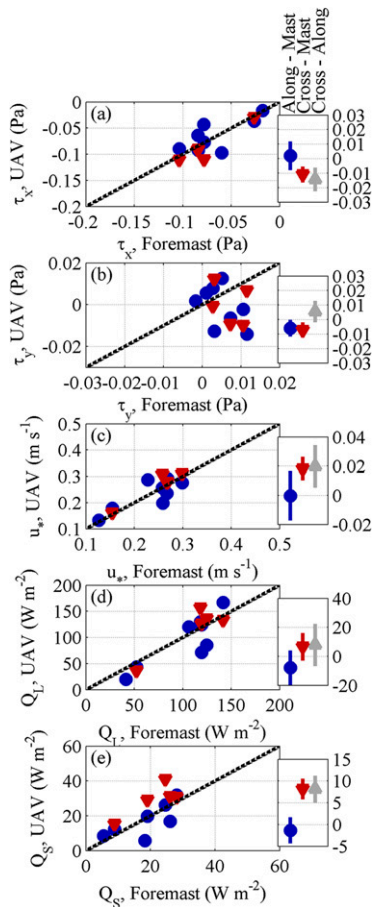


FIG. 14. UAV and foremast one-to-one comparison plots corresponding to Figs. 13a–e. Values are averaged into 6-h bins, with foremast measurements on the abscissa and UAV measurements on the ordinate (along-wind measurements in blue, crosswind measurements in red). Mean differences between the UAV measurements and the foremast measurements are shown in the insets (units match the corresponding plot) for each quantity, with error bars depicting ± 1 standard error. The gray triangles are the difference between cross- and along-wind measurements.

and Thompson 1999). During TW13, we were limited by airspace and other mission priorities, and unfortunately we were not able to pursue these features in detail. The capability of identifying and tracking the evolution of internal waves generated by topography (or subsurface vehicles) across scales of the order of wide continental shelves is of great interest to the oceanographic research community.

b. Previous observations of equatorial internal waves

Narrowband oscillations in the Equatorial Undercurrent, and associated bursts of turbulence well below the ocean surface layer, have been examined by observational (Gregg et al. 1985; Moum et al. 1992b, 2011), numerical (Pham et al. 2012, 2013), and analytical

(Smyth et al. 2011, 2013) studies. These phenomena are the result of high background current shear combined with wind stress and convection. Current research describes two different possible mechanisms for these oscillations: downward-propagating internal waves or intermittent shear instabilities generated and dissipated locally. These phenomena have been previously studied by moored instruments (e.g., Moum et al. 2011), towed vertical arrays, (Moum et al. 1992a), and high-resolution profiling from slowly traversing vessels (S. Nguyen 2014, personal communication). While previous studies estimate wavelengths of around 150–250 m (Moum et al. 1992a), we observe wavelengths in the 400–600-m range, consistent with recent large-eddy simulations with similar stratification (H. Pham 2014, personal communication). For the present study, the features that are coherent in depth and propagate in a manner consistent with mode-1 internal waves in a stratified flow are simply referred to as internal waves.

c. Ship-based observations of equatorial internal waves

To track IW propagation during EquatorMix, space-time ($x-t$) diagrams are generated from horizontal (east–west) sections through the X-band imagery. Two examples are presented in Fig. 17. A running cross correlation between sections is used to estimate phase speed. In the 15 October 2012 sample, IWs are seen to propagate with a westward phase speed of $29 \pm 9 \text{ cm s}^{-1}$, where the uncertainty is estimated as the 1σ distribution of speed estimates over the time range shown in Fig. 17. In contrast, in the 19 October sample, IWs are seen to be quasi stationary in an Earth frame: $0.5 \pm 8.3 \text{ cm s}^{-1}$. These phase speeds are marked with red lines in the $x-t$ diagrams in Figs. 17b,d. They are consistent with the theoretical dispersion relations for these conditions, as discussed in appendix A.

A long spatial series was generated over the 12 h beginning 1800 local time (LT) 18 October by averaging in time between the two dotted red lines. A wavenumber spectrum of this series shows a prominent peak at 440 m (Fig. 18a). These wavelengths and phase speeds are discussed in the context of a theoretical model in the following section. A peak at $\lambda = 440 \text{ m}$ in the spectrum of sea surface temperature for the same 12-h period, measured at $z = -5 \text{ m}$ with the ship's flow-through thermosalinograph (Fig. 18d), is likely associated with the vertical displacement of isotherms due to these internal waves.

A spectrogram of east–west slices from individual 10-min-averaged X-band images (Fig. 3e) reveals a predominantly nocturnal pattern of IW occurrence, which is in agreement with coincident HDSS and

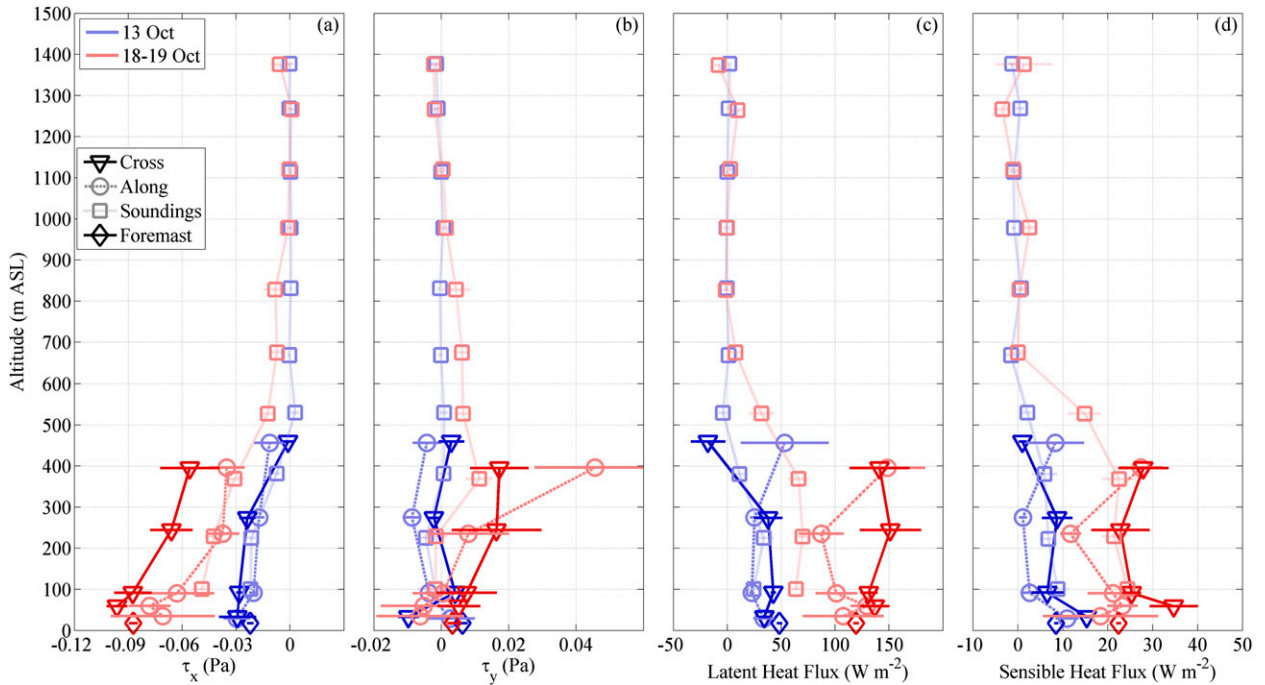


FIG. 15. Vertical profiles of (a) along-wind momentum flux, (b) crosswind momentum flux, (c) latent heat flux, and (d) sensible heat flux, computed from straight-and-level UAV legs (triangles for crosswind, circles for along-wind) and helical soundings (squares), taken near 0°N, 140°W during EquatorMix. Data from two different periods are shown: an 8-h flight starting 0830 LT 13 Oct (blue), and two back-to-back 11-h flights starting at 1208 LT 18 Oct and 0050 19 Oct (red). From 13 to 19 Oct, U_{10} winds increased from 5 to 10 m s^{-1} (Fig. 3). Fluxes from helical soundings are computed from half-orbit segments (1-km diameter) and are averaged into 150-m vertical bins. Error bars for each point show ± 1 standard error. Diamonds mark fluxes computed from the eddy-covariance station on the foremast, with the mean of all 20-min segments over the same period as the corresponding flight(s).

FastCTD data (S. Nguyen 2014, personal communication) and previous studies in this vicinity (Moum et al. 1992a, 2011), suggesting a coupling to surface forcing. Following Ramos et al. (2009), Radon transforms of the time-averaged X-band backscatter are examined from $3.8 \text{ km} \times 1.5 \text{ km}$ boxes upwind of the ship, from which IW direction and wavelength are determined. Westward propagation direction ranged from 260° to 300°, with wavelengths ranging from 400 to 600 m.

d. UAV observations of equatorial internal waves

Three passes of the Flux UAV over the X-band footprint (within 4 km of the *Revelle*) were conducted during EquatorMix. We examine the pass with the most overlap and the most prominent IW features here. Figure 19 shows the X-band footprint and UAV flight track. Filtered and georeferenced X-band imagery has been averaged for 30 min. Recalling from Fig. 17, the IWs at this time were quasi stationary in an Earth frame, and they did not move significantly during the averaging time ($< 10 \text{ m}$, assuming the 0.5 cm s^{-1} phase speed computed in the previous

section). X-band backscatter along the UAV track (the dark gray line in Fig. 19d) is estimated by taking the cross-track mean of the time-averaged backscatter over a 250-m stripe centered on the UAV track. Examining the 50-m bin-averaged lidar backscattered amplitude along this track, there is agreement with the X-band backscatter as may be expected—both are sensitive to the gravity-capillary-scale surface waves that are modulated by the underlying internal wave motion.

Though the Flux payload was equipped with a radiometric sea surface temperature device, the measured variation in surface temperature at the wavelengths associated with internal waves was not significant. Temperature at $z = -5 \text{ m}$, as measured at the shipboard inlet, does show $\pm 0.02^\circ\text{C}$ variations associated with the IWs, and there is a corresponding peak in the spectra as discussed previously (Fig. 18d).

Surface elevation modulations measured with the UAV lidar of around 10–30 cm are seen to be in phase with the X-band signal (Fig. 19d). This signal is also visible in the composite surface elevation spectrum (Fig. 18c) computed from all low-altitude ($\leq 100 \text{ m}$, due

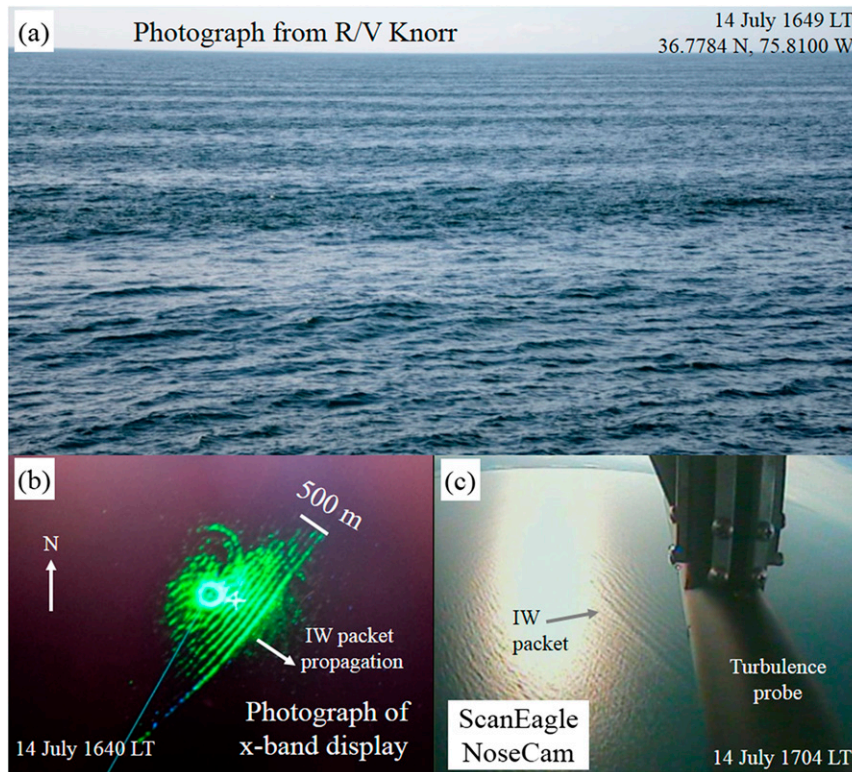


FIG. 16. Internal wave packets as seen during TW13 aboard the R/V *Knorr*. (a) Photograph from 02 deck level of a passing IW packet. The image is a still from a movie, in which these IW packets are seen to slowly propagate away from the ship as surface waves propagate toward the ship. (b) Image of the X-band marine radar display (PPI) 9 min prior to the photograph, from which we estimate a wavelength of about 95 m. (c) Image from the navigation camera of the Flux UAV payload (1000 m MSL), showing an IW packet in the sun glitter. The Virginia coast is at the top of the photograph.

to the range of the lidar) upwind legs in the 12 h starting 18 October 1800 LT. For reference, the Doppler-corrected spectrum is also shown (red curve in Fig. 18c), which accounts for the speed of the UAV in relation to the phase speed of the surface waves. Though there is a peak in coherence between surface elevation and X-band backscatter, it is sensitive to spectral window selection. The area under the surface elevation spectrum's peak at the IW wavelength suggests wave amplitudes on the order of 10 cm, though the spectral width of the peak is much larger than the peak observed in the X-band and current spectra and, consequently, the area depends strongly on the wavenumber range used. Assuming sinusoidal surface elevation, the amplitude ranges from 5 cm for the wavelength band $\lambda = 441 \pm 20$ m to 11 cm for $\lambda = 441 \pm 100$ m (cf. this 120% increase in signal amplitude to only a 38% increase between these same wavelength bands for the X-band spectrum, which has a much narrower peak). This measured amplitude, however, is two to three orders of magnitude larger than the surface amplitudes

predicted by simple mode-1 internal wave solutions. As the lidar-derived elevations are based mainly on precise GPS and time-of-flight measurements, we have more confidence in the observations than in the simplified model, which neglects critical layers and nonlinearities. This discrepancy is discussed further in section 7 and, along with details of the model, in appendix A.

6. Real-time data transmission and assimilation

To the best of our knowledge, the use of ScanEagles during TW13 marked the first use of UAVs for real-time data assimilation into MABL models. A sample 3D trajectory of one 6.5-h flight is presented in Fig. 20. Downsampled (1 Hz) meteorological data from the UAV was transferred during flight from the *Knorr* to the Naval Research Laboratory for assimilation into forecasting models [Coupled Ocean–Atmosphere Mesoscale Prediction System (COAMPS)]. Historically, data from radiosonde balloons are used as

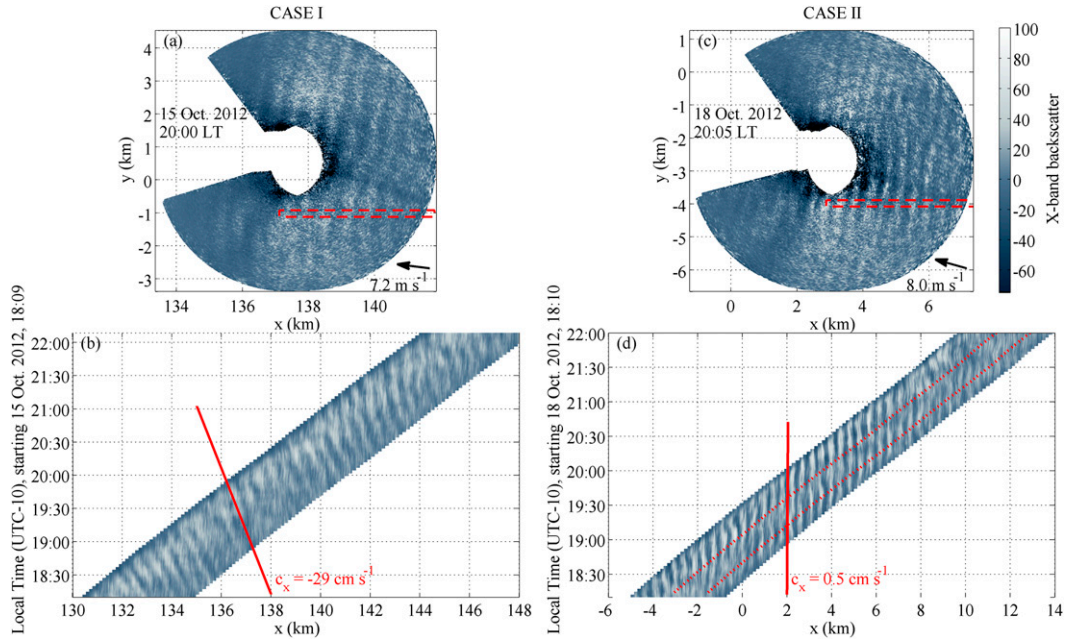


FIG. 17. (a),(c) Sample filtered and averaged georeferenced X-band images and (b),(d) corresponding sections of x - t diagrams for times of persistent crosswind structures associated with IWs observed during EquatorMix. The x - t diagrams are made by extracting the backscattered amplitude within the red box (averaged over the 200-m north-south width) for each time step. At the time of case I (15 Oct 2000 LT), the structures are seen to move westward in an Earth frame at $29 \pm 9 \text{ cm s}^{-1}$ [the slope of the red line in (b)], whereas for case II (18 Oct 2000 LT), propagation of the IWs is near zero ($0.5 \pm 8.3 \text{ cm s}^{-1}$) in an Earth frame. Averaging the backscatter signal in time between the dotted lines in (d), extended to 12 h beginning 1800 LT, gives a long spatial series used for the spectrum in Fig. 18a. Wind direction and speed are given in (a),(c). In both cases, the ship was tracking to the east at 1.0 m s^{-1} .

inputs into these models, but UAVs provide several advantages:

- UAVs are not limited to the airspace directly over ships (nor are they at the whim of the wind), but rather by the range of the platform.
- UAVs can (repeatedly) sample across gradients of atmospheric quantities in regions of high spatial inhomogeneity (e.g., atmospheric fronts).
- UAVs can selectively sample in regions of higher uncertainty (as determined by model sensitivity analysis).
- Near-continuous sampling with UAVs is possible (compared to less-frequent synoptic balloon soundings), which is important in regions of high temporal variability.

Throughout TW13, balloon radiosondes were launched several times per day, intended as “ground truth” points for COAMPS model validation. The radiosondes in this experiment also marked the first opportunity for in situ independent comparisons to the UAV measurements, as discussed in appendix B.

At the payload “ground station” (on the *Knorr*), 10-min files of 1-Hz meteorological data were generated and uploaded via FleetBroadband, within a matter of tens of seconds, to a server at the Scripps Institution of Oceanography

(SIO), which were then accessed by the Naval Research Laboratory (NRL) and assimilated into a regional coupled ocean-atmosphere model. The model was then used by the NRL fleet for radar propagation prediction. An unanticipated technical issue prevented winds from being assimilated in real time; this issue, as well as an error in relative humidity due to a temperature measurement bias, was addressed and corrected in postprocessing.

Analysis of the postprocessed data suggests a substantial improvement of temperature and dewpoint estimation for the UAV data-assimilated case over the nonassimilated case. In the lower 1000 m, the rms error (between the forecast model and balloon radiosonde “truth” profiles) of temperature decreases on average by about 1°C in the assimilated case and the rmse of dewpoint temperature decreases by $1^\circ\text{--}3^\circ\text{C}$ (Doyle et al. 2016). This improvement is concentrated in the vertical vicinity of the top of the atmospheric boundary layer and just above—regions of large wind, temperature, and humidity gradients. Prediction of modified refractivity (a function of temperature and relative humidity, and the important metric in radar propagation; Barclay 2003) is also improved in the assimilated case, suggesting an important operational use of this technology, where

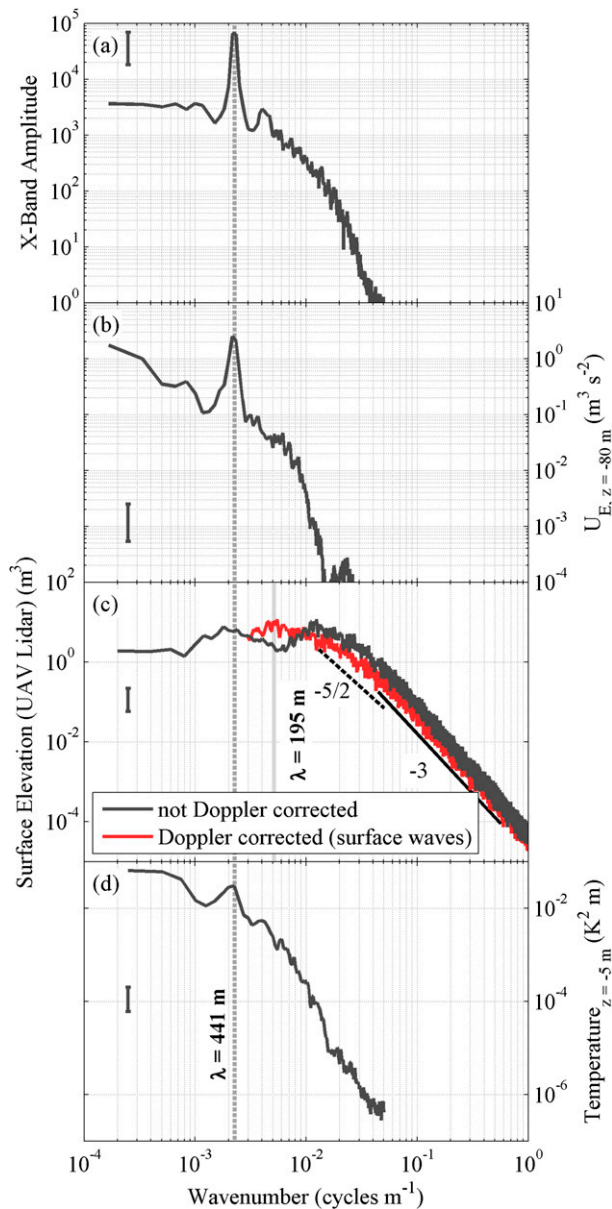


FIG. 18. Wavenumber spectra of (a) along-wind segments of X-band backscattered amplitude, (b) eastward current at a depth of 80 m (computed from the HDSS), (c) UAV lidar-derived surface elevation, and (d) ship thermosalinograph temperature, all showing a peak (or local maximum) at $\lambda = 441$ m. The red line in (c) indicates the Doppler-shifted spectra that account for UAV motion relative to the surface gravity wave speed, assuming a deep-water dispersion relation and unidirectional waves (cropped below $1/330 \text{ m}^{-1}$). All measurements are from the 12 h beginning 1800 LT 18 Oct, while the *Revelle* was traversing to the east at 1 m s^{-1} . The UAV surface wave spectrum (c) is computed from 17 upwind flight segments, each 5 km, at low altitude (30–100 m), all within 15 km of the ship. Vertical bars indicate $\pm 95\%$ confidence intervals.

flights can be concentrated in regions of large gradients or high model uncertainty. Doyle et al. (2016) rigorously quantifies the data assimilation and modeling in the Trident Warrior 2013 experiment leading to these improvements.

7. Discussion

Much as the advent of the aircraft carrier in the first half of the twentieth century allowed navies to “project force” beyond the range of traditional naval vessel operations, UAVs now allow the oceanographic community to “project science” beyond what is feasible with traditional oceanographic vessels. Ship-launched and ship-recovered UAVs permit the study of surface phenomena within the surrounding tens to hundreds of kilometers around the ship, as well as atmospheric sampling up to the altitude limitations of the platform (5 km for the UAVs discussed in this study) or as allowed by local airspace regulations. With data sent back to the ship in real time, scientific missions for the UAV or the ship can be directed “on the fly.” Similarly, information from the ship’s nautical or weather radars permits operators to direct UAV flight paths around areas of interest, for example, atmospheric or oceanic fronts, convective cloud systems, or rainbands. With real-time UAV data assimilation into coupled ocean–atmosphere models, it is conceivable that, in coming years, science missions on research vessels could be influenced or directed by findings from the real-time models, with UAVs (or other platforms), in turn directed toward regions of interest or the highest model uncertainty. This was demonstrated on several occasions during TW13 when logistically feasible.

In this study, we have detailed the use of ship-launched and ship-recovered UAVs from the R/V *Roger Revelle* during the October 2012 Equatorial Mixing experiment and from the R/V *Knorr* during the July 2013 Trident Warrior experiment, and discussed novel measurements of atmospheric structure and ocean surface structures. As far as the authors are aware, the observations discussed in this study represent the first direct air–sea flux measurements from a ship-launched UAV. We are able to identify the presence of longitudinal wind rolls, manifested in a predicted 90° phase shift in vertical and crosswind components. Associated with these rolls, fluxes from crosswind sampling legs were significantly larger (20% for momentum flux, 15% for latent heat, and 55% for sensible heat) than from along-wind sampling legs, including those from the foremast of the vessel. Fluxes are likely being undersampled in along-wind ship tracks, and the typical speeds of the vessels make it difficult to conduct along-wind and crosswind sampling during changing winds. By adding the capability of ship-launched instrumented UAVs

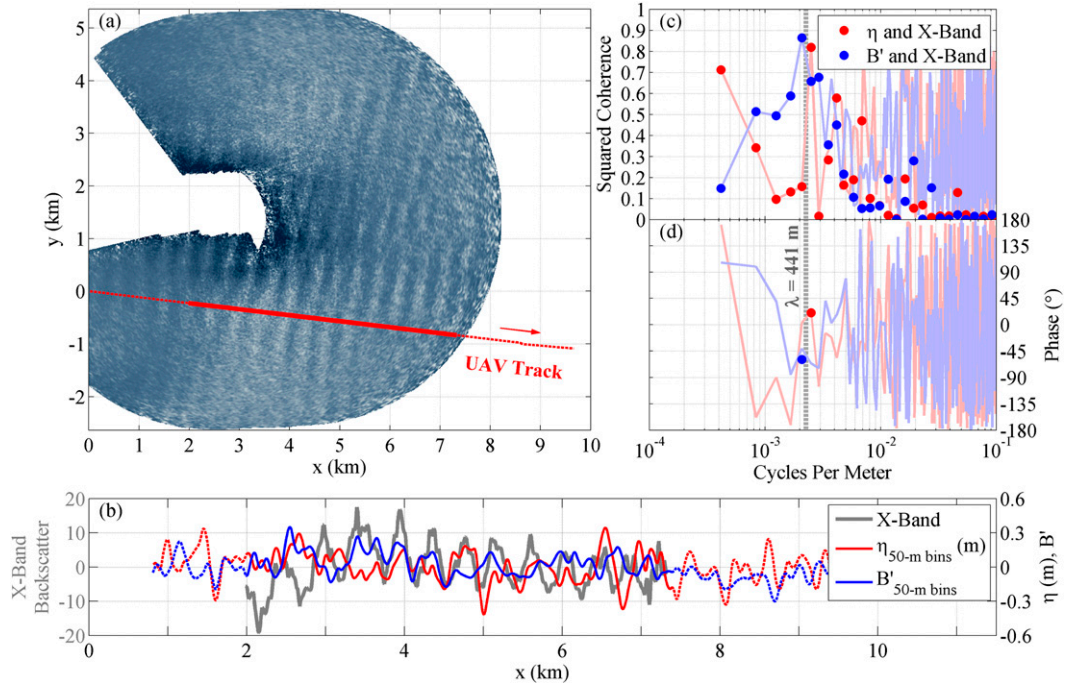


FIG. 19. (a) Flight track of the UAV (1901–1909 LT 18 Oct) over the concurrent X-band footprint averaged over the 30 min starting 1850 LT 18 Oct (overlapping the time of the UAV flight with 11 min on either side). (b) X-band backscatter interpolated along the UAV track, with 50-m running mean of surface elevation (η ; red) and lidar backscatter (B' ; blue) overlaid, as measured from the UAV. Thinner dotted colored lines in (a),(b) indicate UAV data from regions not used in the coherence analysis. (c),(d) Squared coherence and phase between the X-band backscatter and the lidar backscatter (blue) and surface elevation (red) (calculated with spectral windows of 2.4 km), showing peaks in coherence near $\lambda = 441$ m. The solid dots are bin averaged in frequency and are shown only in (d) where the squared coherence is over 0.8. A small negative phase between lidar backscatter and X-band backscatter [blue mark in (d)] corresponds to a small shift of the X-band backscatter to the left ($-x$) of the lidar backscattered amplitude.

instrumented for accurate flux measurements, this problem could be mitigated in the future.

UAV imagery and lidar permit detection of surface signatures of processes within the water column. Slight

modulations in surface roughness due to variations in $O(1)$ -cm gravity–capillary waves are measurable by variations in the backscattered intensity of lidar data. With data from EquatorMix, we have shown coherence

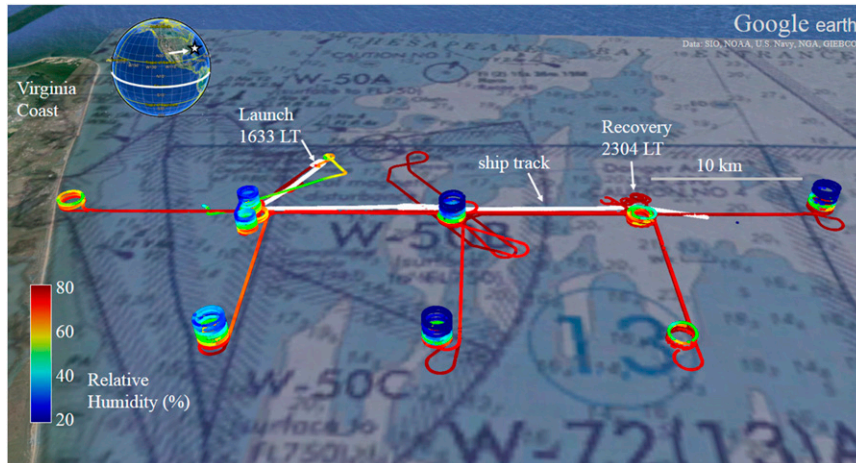


FIG. 20. Sample 1-Hz real-time data in Google Earth during one 6.5-h UAV flight during TW13 (36.8°N, 75.7°W), starting 1633 LT (UTC – 4 h) 14 Jul 2013. Winds for this time, as measured from the ship, were 4–5 m s^{-1} from the east. An aeronautical chart is overlaid on the surface.

between the UAV lidar backscatter and the X-band backscatter modulations at the wavelengths associated with internal waves during an overlapping UAV pass. Additionally, there are coherent fluctuations in lidar-derived surface elevation, with amplitudes much larger than predicted by linear internal wave–current interaction theory. We have more confidence in the measurements from the UAV than the simple internal wave model used for comparison, which did not include critical layers nor nonlinearity, but it appears to have accounted for the kinematics of the waves to leading order (the dispersion relationship) but not the dynamics (the amplitudes). The UAV measurements were primarily very accurate time or time-of-flight measurements by the GPS and lidar systems. The comparison should motivate more studies of these surface signatures and the underlying dynamics.

The successful use of the UAV operations in both the EquatorMix and Trident Warrior 2013 experiments is an important milestone in the use of unmanned vehicles in atmospheric and physical oceanographic research. Low-altitude flights permit accurate air–sea flux measurements over large spatial scales for extended periods of time, without introducing any significant human risk. The main benefits over manned aircraft research flights also include the reduction or elimination of transit times and the opening of central oceanic basins to long-duration, near-continuous studies. UAVs can be important in observing and characterizing larger atmospheric structures not observable in situ by slowly moving ships, especially ships traversing upwind, as is a common strategy for reducing errors due to vessel flow distortion. The two experiments demonstrated that UAVs can be integrated into larger field programs, providing important spatial measurements of the atmosphere and ocean surface, while ship-based observations can provide complementary high-resolution measurements in depth and time. Ship-launched UAVs, sampling the MABL and ocean surface, greatly extend the scientific reach of a research vessel, and, especially when combined with ship-based surface and subsurface instrumentation, can be used to explore many oceanographic and MABL phenomena.

Acknowledgments. Nicholas Statom was instrumental in the UAV payload design and science operations, as was Daniel Bedenko in electronics design and integration. We are grateful to San Nguyen and Robert Pinkel for providing mean CTD profiles from EquatorMix. Thanks to EquatorMix Chief Scientist Jerome Smith. Thanks to James Doyle, Marine Meteorology Division of the NRL, for discussions of ScanEagle data assimilation results, and to Daniel Eleuterio for his support throughout TW13.

We thank ScanEagle pilots and operators Lorenz Eber, Cyrus Roohi, Trevor Layh, Laura San Filippo,

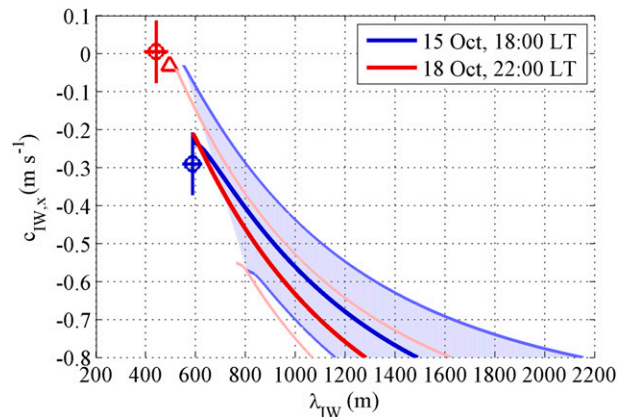


FIG. A1. Dispersion relations (wavelength vs phase speed) for mode-1 IWs given different stratifications from two different times (red, blue). Thick lines are model results using the mean surface current determined from WaMoS during 13–19 Oct 2012 (-0.25 m s^{-1}), while the lower and upper thinner lines are calculated for the lower and upper surface current estimates for this period ($-0.64, 0.32 \text{ m s}^{-1}$, respectively). Only model solutions without critical layers are presented. Circles are the observed wavelengths and phase speeds using the X-band data presented in Fig. 17. Error bars in sample observed phase speed and wavelength are the 1σ distribution of wavelengths and phase speeds determined from cross and autocorrelations. The triangle is the model presented in Figure A2.

Adam Broad, Jonathan Elliott, and Richard Lay (NSWCDD). Arunav Sarkar, Alexander Chang, and Timothy Wheeler helped to develop the graphical interface for the ScanEagle real-time scientific data display. We thank Eric Terrill, Tony de Paolo, and Tom Cook for providing X-band data. Thanks to Katherine Horgan and Victor Wiss (NSWCDD), and to Peter Guest (NPS), for collecting and quality controlling the radiosonde profiles used in this study, and to the captains and crews of the *Revelle* and *Knorr* for their support during the field campaigns.

This research was supported by grants to WKM from the Office of Naval Research (N00014-11-1-0790, N00014-11-1-0368, and N00014-13-1-0193). Any requests for data are to be addressed to W. K. Melville.

APPENDIX A

Comparison of Internal Wave Observations and Theory

To analyze the equatorial internal waves seen during EquatorMix, we construct a linearized eigenvalue problem. Given mean profiles of current $U(z)$ and buoyancy frequency $N(z)$ internal wave modes are calculated using the form of the Taylor–Goldstein equation derived in Kundu et al. (2012):

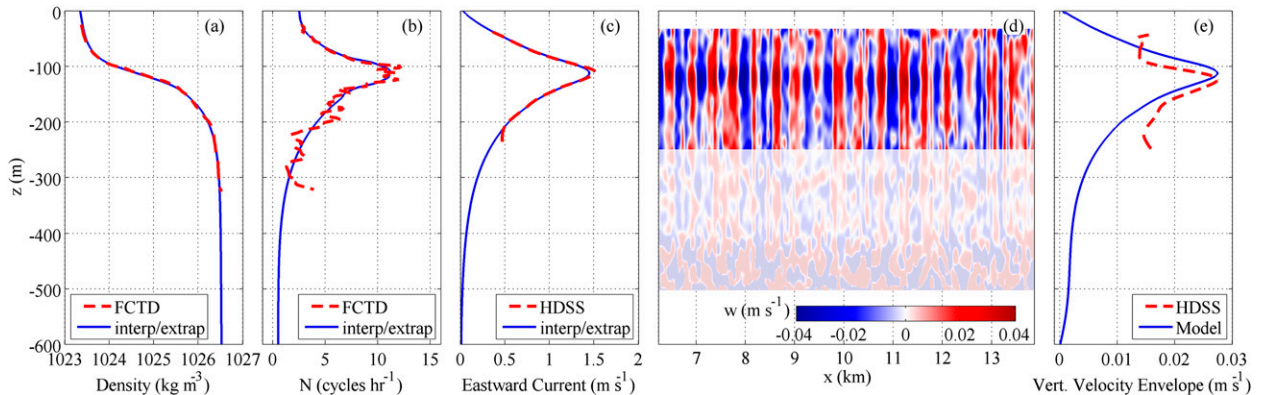


FIG. A2. Average (a) density and (b) buoyancy frequency measured with the fastCTD, (c) mean eastward current measured with the HDSS, (d) filtered vertical velocity profiles w_f from the HDSS, and (e) theoretical mode-1 IW (blue) and measured (red) vertical velocity envelope, all for 2000–2200 LT 18 Oct 2012. The maximum of the model vertical velocity envelope is prescribed as the peak of the measured envelope. Data below 250 m are masked off in (d).

$$(U - c) \left(\frac{d^2}{dz^2} - k^2 \right) \hat{\psi} - \frac{d^2 U}{dz^2} \hat{\psi} + \frac{N^2}{U - c} \hat{\psi} = 0, \quad (\text{A1})$$

where $\hat{\psi}$ is the vertical structure of streamfunction ψ (with velocity components $u = U(z) + \partial\psi/\partial z$, $w = -\partial\psi/\partial x$), which is assumed to have wavelike behavior in x and t , $\psi(x, z, t) = \hat{\psi}(z) \exp[ik(x - ct)]$, and c is the phase speed. A separate IW mode solver, written by W. Smyth (and available online at <http://salty.oce.orst.edu/>; see Smyth et al. 2011, their appendix A), is used to verify the solutions.

We approximate the internal waves as two-dimensional, in the $+x$ (east) and $+z$ (vertical) planes. The eastward current profile is adapted from a 2-h mean of the *Revelle's* HDSS, with a decaying exponential fit below 210 m. Above 30 m, the current is extrapolated to a specified surface current. Surface current (unavailable from the HDSS) is nominally determined from the WaMoS/X-band radar system, which uses the observed shift of surface waves from the deep-water dispersion relation to calculate a mean surface current (Nieto Borge et al. 2004). A 12-m smoothing is then applied in depth. Density profiles are determined from hourly means of fastCTD profiles, with a decaying exponential in squared buoyancy frequency N^2 below 150 m, set to $N = 0.5$ cph at $z = -600$ m. A 9-m smoothing is applied in depth.

Given these currents and buoyancy profiles, mode-1 solutions are computed with small westward phase speeds ($-0.8 \text{ m s}^{-1} \leq c \leq 0.0 \text{ m s}^{-1}$) and wavelengths of 450–1500 m. Figure A1 presents sample modeled dispersion relations (phase speed vs wavelength) for two observed stratifications during EquatorMix. The two observed test cases from Fig. 17 are superimposed. The surface current from WaMoS is considered a preliminary product, especially in regions of expected

high shear.⁴ Because of the sensitivity of the model to the upper-ocean current profile, a range of surface current speeds are considered, based on the range of currents estimated by WaMoS for that surrounding week of data (-0.64 to 0.32 m s^{-1}). Additionally, only profiles with no critical layers (depths at which phase speed equals current speed) are considered, which accounts for the cropping of the dispersion curves at higher (more positive) phase speeds (Smyth et al. 2011).

Figure A2 shows sample depth profiles of density, buoyancy frequency, eastward and vertical currents, and the corresponding mode-1 solutions using the solvers described above for the 2 h beginning 2100 LT 18 October 2012—a period of strong surface and subsurface evidence of internal wave activity. Note the mode-1 IWs visible in the depth-versus-time contour plot of filtered vertical velocity w_f , which has been high-pass filtered in the along-track direction with a cutoff of 2 km and low-pass filtered in depth with a cutoff of 20 m. The HDSS vertical velocity envelope (Fig. A2e) is determined, assuming a sinusoidal velocity, as

$$\hat{w}_{\text{HDSS}}(z) = (2 \langle w_f(x, z)^2 \rangle)^{1/2}, \quad (\text{A2})$$

where angle brackets indicate averaging in x along each depth interval over the 2 h shown in Fig. A2d. During this time, the IWs are seen to be nearly stationary in an Earth frame (recalling Fig. 17d), which agrees with the -3 cm s^{-1} phase speed of the numerical solutions.

While this analysis has several limitations (linear, two-dimensional model, no critical layers, and an uncertain surface current input), it suggests that the wavelengths and phase speeds observed in the X-band and UAV data

⁴ Methods for deriving depth-shear profiles from sequences of X-band imagery are under development (Campana et al. 2016).

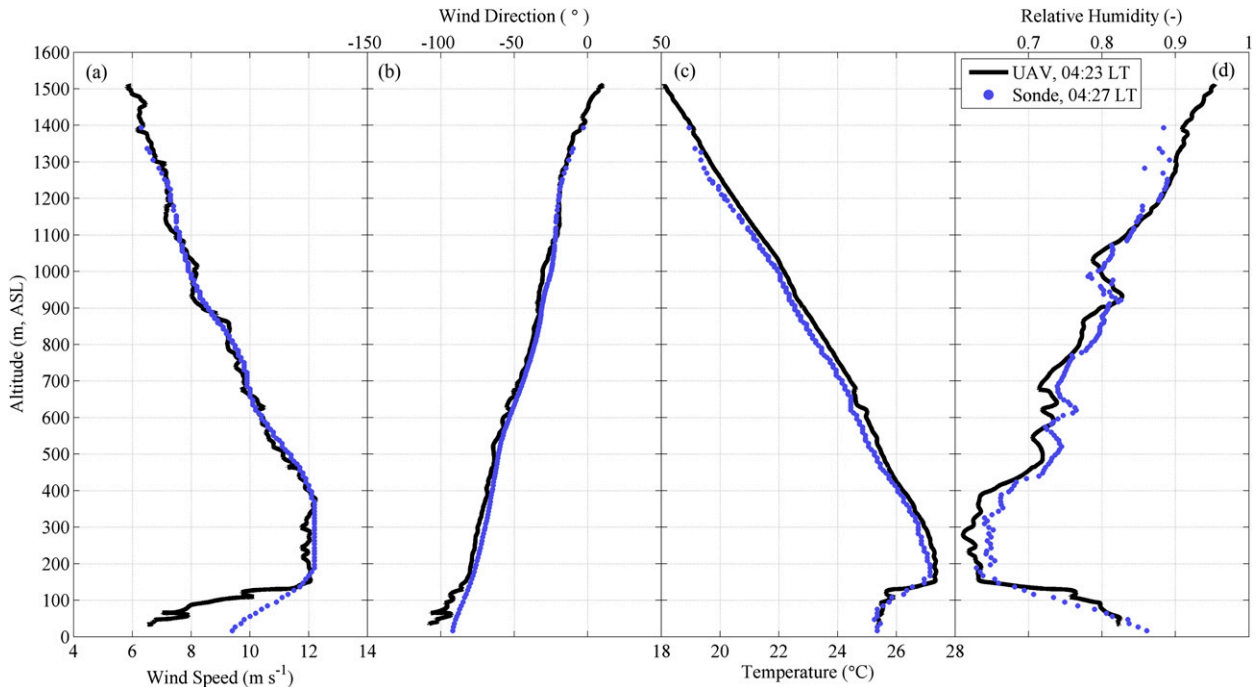


FIG. B1. Profile comparison between balloon radiosonde (blue) and UAV Flux payload (black), showing (a) wind speed, (b) wind direction, (c) temperature, and (d) relative humidity. These soundings were performed during TW13, at 36.70°N, 75.79°W. Local times (UTC - 4 h) on the morning of 16 Jul 2013 are given. A strong temperature inversion is notable at about 130 m. The discrepancy in wind speeds below 120 m is discussed in the text.

are within the range of values estimated using the analytical model.

Though the model assumes a rigid lid, we can estimate the sea surface height anomaly (SSHA) by assuming a hydrostatic water column near the surface (Gill 1982; Zhao et al. 2010). We first follow the polarization relations presented in Smyth et al. (2011), neglecting viscosity, to compute the pressure modulation envelope:

$$\hat{P}(z) = \frac{\rho g}{k} [U_z \hat{w} + (c - U) \hat{w}_z] + C, \quad (\text{A3})$$

where $\hat{w}(z)$ is vertical velocity envelope, $U(z)$ is mean eastward current, c is phase speed, ρ is density, g is acceleration due to gravity, k is wavenumber, and constant C is selected such that the depth-averaged pressure modulation is zero: $\int_{z=-600\text{m}}^0 \hat{P}(z) dz = 0$ (Zhao et al. 2010). Pressure, like velocity, is assumed to have wave-like behavior, that is, $P(x, z, t) = \hat{P}(z) \exp[ik(x - ct)]$. The vertical velocity modulation envelope of the mode-1 solution $\hat{w}(z)$ is scaled such that the peak value equals the peak value observed in the HDSS data [from (A2)] (Fig. A2e). Sea surface height anomaly is then computed using the pressure at the surface:

$$\text{SSHA} = \frac{P_{z=0}}{\rho_0 g}. \quad (\text{A4})$$

By this method, surface elevation fluctuations for the stratification and wavelengths observed during this experiment are predicted to be on the order of 0.1–1 mm—two to three orders of magnitude smaller than the fluctuations observed by the UAV lidar, as discussed in section 5d. We do not believe the large [$O(10)$ cm] signal measured by the UAV lidar to be a result of errors in GPS positioning or lidar point georeferencing, as the signal is not evident in spectra of UAV altitude or attitude, and is larger than the 2–3-cm accuracy estimated by the system for 50-m binning.⁵

Internal wave–induced surface elevation modulations from airborne lidar have recently been examined by Magalhaes et al. (2013), but the approximately 1-m change in relative scattering lidar height around the IW crest observed in that study is attributed to possible multiple reflections in surfactant foam.⁶ Additional

⁵ Given uncorrelated error sources, accuracy is assumed to scale by $r^{-1/2}$, where r is the ratio of samples—or in this case, bin sizes. In Reineman et al. (2013), accuracy was determined to be 9 cm for 4-m bins, giving 2.5 cm for 50-m bins.

⁶ It is the opinion of the authors of the present study that this change in scattering height measured by Magalhaes et al. (2013) is likely instead due to erroneous target detection of the digitized reflected light signal at regions of brighter reflectance.

work is needed to determine a physical explanation for the discrepancy between measured and predicted surface elevations in the present study.

APPENDIX B

UAV Comparison with Radiosonde Balloons

During Trident Warrior 2013, balloon radiosondes were launched both synoptically (every 6 h) and in conjunction with nearby UAV soundings. Radiosondes were operated by investigators from the Naval Postgraduate School (synoptic soundings, ascending only) and by the Naval Surface Warfare Center, Dahlgren Division (“up–down” soundings). Over the 5 days of the experiment, there were 18 synoptic sondes launched and 30 additional sondes around and during UAV flights. The radiosondes were mainly intended as ground truth points for COAMPS model validation.

The radiosondes in this experiment also marked the first opportunity for in situ independent comparisons to the UAV measurements (no balloon soundings were performed during EquatorMix). Root-mean-square differences in wind, temperature, and relative humidity between UAV and radiosonde measurements during two flights on a typical day are $0.4\text{--}0.8\text{ m s}^{-1}$, $0.2^\circ\text{--}0.3^\circ\text{C}$, and $2\%\text{--}4\%$, respectively (“collocated” soundings of balloon and UAV profiles are within 30 min of each other and less than 15 km apart).

Figure B1 shows a sample comparison of a vertical sounding from the UAV with that of a descending balloon radiosonde 11.5 km away. The discrepancy of wind measurements in the high-shear region below 120 m is arguably partly due to the altitude difference between the balloon and the sensor: the speed of the balloon (and sensor) follows the wind speed at the height of the balloon, while the sensor records the GPS altitude 30 m down the tether.

REFERENCES

- Barclay, L., Ed., 2003: *Propagation of Radiowaves*. 2nd ed. Electromagnetic Wave Series, Vol. 502, Institution of Electrical Engineers, 480 pp.
- Bell, P. S., 1999: Shallow water bathymetry derived from an analysis of X-band marine radar images of waves. *Coastal Eng.*, **37**, 513–527, doi:10.1016/S0378-3839(99)00041-1.
- Brooks, I., and D. Rogers, 1997: Aircraft observations of boundary layer rolls off the coast of California. *J. Atmos. Sci.*, **54**, 1834–1849, doi:10.1175/1520-0469(1997)054<1834:AOBLR>2.0.CO;2.
- Brown, R. A., 1970: A secondary flow model for the planetary boundary layer. *J. Atmos. Sci.*, **27**, 742–757, doi:10.1175/1520-0469(1970)027<0742:ASFMFT>2.0.CO;2.
- Campana, J., E. J. Terrill, and T. de Paolo, 2016: The development of an inversion technique to extract vertical current profiles from X-band radar observations. *J. Atmos. Oceanic Technol.*, doi:10.1175/JTECH-D-15-0145.1, in press.
- Chen, W., M. Banner, E. Walsh, J. Jensen, and S. Lee, 2001: The Southern Ocean Waves Experiment. Part II: Sea surface response to wind speed and wind stress variations. *J. Phys. Oceanogr.*, **31**, 174–198, doi:10.1175/1520-0485(2001)031<0174:TSOWEP>2.0.CO;2.
- de Sousa, J., P. McGuillivray, J. Vicente, M. Nunes Bento, J. A. P. Morgado, M. Madruga Matos, R. Ayres Gomes Bencatel, and P. Mónica de Oliveira, 2014: Unmanned aircraft systems for maritime operations. *Handbook of Unmanned Aerial Vehicles*, K. P. Valavanis and G. J. Vachtsevanos, Eds., Springer, 2787–2811, doi:10.1007/978-90-481-9707-1_75.
- Dillon, T., J. Moum, T. Chereskin, and D. Caldwell, 1989: Zonal momentum balance at the equator. *J. Phys. Oceanogr.*, **19**, 561–570, doi:10.1175/1520-0485(1989)019<0561:ZMBATE>2.0.CO;2.
- Doyle, J. D., T. R. Hold, and D. D. Flagg, Eds., 2016: Trident Warrior 2013. NRL Tech. Memo. PAO 16-1231-2460, 241 pp.
- Edson, J. B., A. A. Hinton, K. E. Prada, J. E. Hare, and C. W. Fairall, 1998: Direct covariance flux estimates from mobile platforms at sea. *J. Atmos. Oceanic Technol.*, **15**, 547–562, doi:10.1175/1520-0426(1998)015<0547:DCFEFM>2.0.CO;2.
- Etling, D., and R. Brown, 1993: Roll vortices in the planetary boundary layer: A review. *Bound.-Layer Meteor.*, **65**, 215–248, doi:10.1007/BF00705527.
- Fairall, C., E. Bradley, D. Rogers, J. Edson, and G. Young, 1996: Bulk parameterization of air-sea fluxes for Tropical Ocean-Global Atmosphere Coupled-Ocean Atmosphere Response Experiment. *J. Geophys. Res.*, **101**, 3747–3764, doi:10.1029/95JC03205.
- Friehe, C. A., and Coauthors, 1991: Air-sea fluxes and surface layer turbulence around a sea surface temperature front. *J. Geophys. Res.*, **96**, 8593–8609, doi:10.1029/90JC02062.
- Gee, J., S. Cande, D. Kent, R. Partner, and K. Heckman, 2008: Mapping geomagnetic field variations with unmanned airborne vehicles. *Eos, Trans. Amer. Geophys. Union*, **89**, 178–179, doi:10.1029/2008EO190002.
- Gill, A., 1982: *Atmosphere–Ocean Dynamics*. Academic Press, 662 pp.
- Gregg, M., H. Peters, J. Wesson, N. Oakey, and T. Shay, 1985: Intensive measurements of turbulence and shear in the equatorial undercurrent. *Nature*, **318**, 140–144, doi:10.1038/318140a0.
- Hein, P., and R. Brown, 1988: Observations of longitudinal roll vortices during arctic cold air outbreaks over open water. *Bound.-Layer Meteor.*, **45**, 177–199, doi:10.1007/BF00120822.
- Hessner, K., K. Reichert, J. C. Nieto Borge, C. L. Stevens, and M. J. Smith, 2014: High-resolution X-band radar measurements of currents, bathymetry and sea state in highly inhomogeneous coastal areas. *Ocean Dyn.*, **64**, 989–998, doi:10.1007/s10236-014-0724-7.
- Jackson, C., 2007: Internal wave detection using the Moderate Resolution Imaging Spectroradiometer (MODIS). *J. Geophys. Res.*, **112**, C11012, doi:10.1029/2007JC004220.
- Jones, I. S. F., and Y. Toba, 2001: *Wind Stress over the Ocean*. Cambridge University Press, 326 pp.
- Kelly, R. D., 1984: Horizontal roll and boundary-layer interrelationships observed over Lake Michigan. *J. Atmos. Sci.*, **41**, 1816–1826, doi:10.1175/1520-0469(1984)041<1816:HRABLI>2.0.CO;2.
- Kundu, P. K., I. M. Cohen, and D. H. Dowling, 2012: *Fluid Mechanics*. 4th ed. Elsevier Science, 904 pp.

- Lund, B., H. C. Graber, J. Xue, and R. Romeiser, 2013: Analysis of internal wave signatures in marine radar data. *IEEE Trans. Geosci. Remote Sens.*, **51**, 4840–4852, doi:10.1109/TGRS.2012.2230635.
- Magalhaes, J., J. Silva, M. Batista, L. Gostiaux, T. Gerkema, A. New, and D. Jeans, 2013: On the detectability of internal waves by an imaging lidar. *Geophys. Res. Lett.*, **40**, 3429–3434, doi:10.1002/grl.50669.
- Moum, J. N., D. Hebert, C. Paulson, and D. Caldwell, 1992a: Turbulence and internal waves at the equator. Part I: Statistics from towed thermistors and a microstructure profiler. *J. Phys. Oceanogr.*, **22**, 1330–1345, doi:10.1175/1520-0485(1992)022<1330:TAIWAT>2.0.CO;2.
- , —, —, —, M. McPhaden, and H. Peters, 1992b: Internal waves, dynamic instabilities, and turbulence in the equatorial thermocline: An introduction to three papers in this issue. *J. Phys. Oceanogr.*, **22**, 1357–1359, doi:10.1175/1520-0485(1992)022<1357:IWDIAT>2.0.CO;2.
- , J. D. Nash, and W. D. Smyth, 2011: Narrowband oscillations in the upper equatorial ocean. Part I: Interpretation as shear instabilities. *J. Phys. Oceanogr.*, **41**, 397–411, doi:10.1175/2010JPO4450.1.
- Nieto Borge, J. C., G. Rodríguez Rodríguez, K. Hessner, and P. Izquierdo González, 2004: Inversion of marine radar images for surface wave analysis. *J. Atmos. Oceanic Technol.*, **21**, 1291–1300, doi:10.1175/1520-0426(2004)021<1291:IOMRIF>2.0.CO;2.
- Oost, W. A., C. W. Fairall, J. B. Edson, S. D. Smith, R. J. Anderson, J. A. Wills, K. B. Katsaros, and J. DeCosmo, 1994: Flow distortion calculations and their application in HEXMAX. *J. Atmos. Oceanic Technol.*, **11**, 366–386, doi:10.1175/1520-0426(1994)011<0366:FDCATA>2.0.CO;2.
- Pham, H. T., S. Sarkar, and K. B. Winters, 2012: Near-*N* oscillations and deep-cycle turbulence in an upper-equatorial undercurrent model. *J. Phys. Oceanogr.*, **42**, 2169–2184, doi:10.1175/JPO-D-11-0233.1.
- , —, and —, 2013: Large-eddy simulation of deep-cycle turbulence in an equatorial undercurrent model. *J. Phys. Oceanogr.*, **43**, 2490–2502, doi:10.1175/JPO-D-13-016.1.
- Pinkel, R., L. Rainville, E. Slater, A. Goldin, L. Green, M. Bui, and T. Aja, 2003: The hydrographic Doppler sonar system on the Roger Revelle. *Proceedings of the IEEE/OES Seventh Working Conference on Current Measurement Technology*, IEEE, 237–239, doi:10.1109/CCM.2003.1194320.
- Porter, D., and D. Thompson, 1999: Continental shelf parameters inferred from SAR internal wave observations. *J. Atmos. Oceanic Technol.*, **16**, 475–487, doi:10.1175/1520-0426(1999)016<0475:CSPIFS>2.0.CO;2.
- Rainville, L., and R. Pinkel, 2006: Baroclinic energy flux at the Hawaiian Ridge: Observations from the R/P *FLIP*. *J. Phys. Oceanogr.*, **36**, 1104–1122, doi:10.1175/JPO2882.1.
- Ramos, R. J., B. Lund, and H. C. Graber, 2009: Determination of internal wave properties from X-band radar observations. *Ocean Eng.*, **36**, 1039–1047, doi:10.1016/j.oceaneng.2009.07.004.
- Reineman, B. D., 2013: The development of instrumentation and methods for measurement of air-sea interaction and coastal processes from manned and unmanned aircraft. Ph.D. dissertation, Scripps Institution of Oceanography, University of California, San Diego, 182 pp.
- , L. Lenain, D. Castel, and W. K. Melville, 2009: A portable airborne scanning lidar system for ocean and coastal applications. *J. Atmos. Oceanic Technol.*, **26**, 2626–2641, doi:10.1175/2009JTECHO703.1.
- , —, N. M. Statom, and W. K. Melville, 2013: Development and testing of instrumentation for UAV-based flux measurements within terrestrial and marine atmospheric boundary layers. *J. Atmos. Oceanic Technol.*, **30**, 1295–1319, doi:10.1175/JTECH-D-12-00176.1.
- Sikora, T. D., and S. Ufermann, 2004: Marine atmospheric boundary layer cellular convection and longitudinal roll vortices. Synthetic aperture radar marine user's manual, C. R. Jackson and J. R. Apel, Eds., NOAA, 321–330.
- Smyth, W. D., J. N. Moum, and J. D. Nash, 2011: Narrowband oscillations in the upper equatorial ocean. Part II: Properties of shear instabilities. *J. Phys. Oceanogr.*, **41**, 412–428, doi:10.1175/2010JPO4451.1.
- , —, L. Li, and S. Thorpe, 2013: Diurnal shear instability, the descent of the surface shear layer, and the deep cycle of equatorial turbulence. *J. Phys. Oceanogr.*, **43**, 2432–2455, doi:10.1175/JPO-D-13-089.1.
- Sullivan, P. P., J. C. McWilliams, and E. G. Patton, 2014: Large-eddy simulation of marine atmospheric boundary layers above a spectrum of moving waves. *J. Atmos. Sci.*, **71**, 4001–4027, doi:10.1175/JAS-D-14-0095.1.
- Wang, C., and R. Pawlowicz, 2012: Oblique wave-wave interactions of nonlinear near-surface internal waves in the Strait of Georgia. *J. Geophys. Res.*, **117**, C06031, doi:10.1029/2012JC008022.
- Webb, E., G. Pearman, and R. Leuning, 1980: Correction of flux measurements for density effects due to heat and water vapour transfer. *Quart. J. Roy. Meteor. Soc.*, **106**, 85–100, doi:10.1002/qj.49710644707.
- Yelland, M., B. Moat, P. Taylor, R. Pascal, J. Hutchings, and V. Cornell, 1998: Wind stress measurements from the open ocean corrected for airflow distortion by the ship. *J. Phys. Oceanogr.*, **28**, 1511–1526, doi:10.1175/1520-0485(1998)028<1511:WSMFTO>2.0.CO;2.
- Zhao, Z., M. H. Alford, J. A. MacKinnon, and R. Pinkel, 2010: Long-range propagation of the semidiurnal internal tide from the Hawaiian Ridge. *J. Phys. Oceanogr.*, **40**, 713–736, doi:10.1175/2009JPO4207.1.